Control of radiation and evaporation on temperature variability in a WRF regional climate simulation: comparison with colocated long term ground based observations near Paris

Sophie Bastin, Marjolaine Chiriaco, Philippe Drobinski

Control of radiation and evaporation on temperature variability in a WRF regional climate simulation: comparison with colocated long term ground based observations near Paris

Bastin S.[(1)*], Chiriaco M.[(1)], Drobinski P.[(2)]

(1) Université Versailles St-Quentin, Université Paris-Saclay ; Sorbonne Universités, UPMC Univ. Paris 06 ; CNRS/INSU, LATMOS-IPSL, 11 bd d'Alembert, 78280 Guyancourt, France.

(2) Laboratoire de Météorologie Dynamique, Ecole Polytechnique, Sorbonne Universités, UPMC Univ. Paris 06 ; CNRS/INSU, 91128 Palaiseau, France

* Corresponding author: sophie.bastin@latmos.ipsl.fr; +33180285232

Acknowledgments This work is a contribution to the HyMeX program (HYdrological cycle in The Mediterranean EXperiment) through INSU-MISTRALS support and the MEDCORDEX program (COordinated Regional climate Downscaling EXperiment - Mediterranean region). This research has received funding from the French National Research Agency (ANR) projects REMEMBER (grant ANR-12-SENV-001). It was supported by the IPSL group for regional climate and environmental studies, with granted access to the HPC resources of GENCI/IDRIS (under allocation i2011010227). The SIRTA-ReOBS effort also benefited from the support of the L-IPSL funded by ANR under the "Programme d'Investissements d'Avenir (grant ANR-10-LABX-0018) and by the EUCLIPSE project funded by the European Commission under the Seventh Framework Program (grant n°244067). We would like to ackowledge the SIRTA and Climserv teams at IPSL for collecting and providing data and computing ressources; Cindy Lebeaupin-Brossier and Marc Stefanon for providing simulation outputs; the CNES (Centre National d'Etudes Spatiales) for partially funded M. Chiriaco research.

Abstract:

The objective of this paper is to understand how large-scale processes, cloud cover and surface fluxes affect the temperature variability over the SIRTA site, near Paris, and in a regional climate simulation performed in the frame of HyMeX/Med-CORDEX programs. This site is located in a climatic transitional area where models usually show strong dispersions despite the significant influence of large scale on interannual variability due to its western location. At seasonal time scale, the temperature is mainly controlled by surface fluxes. In the model, the transition from radiation to soil moisture limited regime occurs earlier than in observations leading to an overestimate of summertime temperature. An overestimate of shortwave radiation (SW), consistent with a lack of low clouds, enhances the soil dryness. A simulation with a wet soil is used to better analyse the relationship between dry soil and clouds but while the wetter soil leads to colder temperature, the cloud cover during daytime is not increased due to the atmopsheric stability.

At shorter time scales, the control of surface radiation becomes higher. In the simulation, higher temperatures are associated with higher SW. A wet soil mitigates the effect of radiation due to modulation by evaporation. In observations, the variability of clouds and their effect on SW is stronger leading to a nearly constant mean SW when sorted by temperature quantile but a stronger impact of cloud cover on day-to-day temperature variability. Impact of cloud albedo effect on precipitation is also compared.

Key-words: Hymex, CORDEX, temperature variability, SIRTA-ReOBS, surface and radiative fluxes, lidar simulator, cloud radiative effects, land surface-atmosphere interactions.

1. Introduction:

In the context of climate change, the European mean temperature and its summer variability are predicted to increase compared to the present-day conditions (Giorgi et al., 2006; Fisher and Schär, 2009), and this would increase the probability of occurrence of extreme events similar to the heat wave of summer 2003 (Schär et al., 2004; Nogaj et al., 2006), but also their intensity and duration (Gao et al., 2006; Della-Marta et al., 2007). However, despite extreme events are of particular scientific interest due to their brutal societal and environmental impacts (e.g Vautard et al., 2007; Fink et al., 2004), the temperature variability at all time scales (decadal, inter-annual, seasonal, diurnal) also influences human society in numerous sectors of activity including energy production, health, agriculture and more generally economy and ecology. A good characterization and predictability of the temperature variability then helps the population and stakeholders to anticipate and adapt to extreme events and future climate, and helps to estimate air quality (Vautard et al., 2011; Menut, 2003), energy production and eco and agro-systems evolution.

Temperature variability over Europe is influenced by combined effects of i) large scale dynamics which determine the advection of air masses from Atlantique, North-Africa, Artic/Scandinavia or continental Asia (e.g Xoplaki et al., 2004), and ii) regional scale processes including land surface-atmosphere interactions, cloud-radiation feedbacks and boundary layer processes. The leading drivers of temperature variability are specific for each season and depend on the considered time scale (e.g Vautard and Yiou, 2009; Ionita et al., 2012a,b, 2015; Cattiaux et al., 2011). European climate is particularly sensitive to the interactions between cloud-radiation and surface-atmosphere feedbacks which cause large uncertainty in the prediction of future climate (Hawkins and Sutton, 2009; Cheruy et al., 2014). Over southern areas (Mediterranean surrounding areas), evapotranspiration is limited and controlled by soil dryness (Seneviratne et al., 2010): this is the soil-moisture limited regime, where a positive feedback loop can be generated, drier soils leading to warmer and drier air, which may prevent clouds to form thus enhancing shortwave radiation at surface which causes even more drying of the soil. Over northern countries (Scandinavia), where the soil is wetter, the solar radiation is reduced due to high latitudes leading to the limitation of evapotranspiration by energy availability (Teuling et al., 2009): an increase of solar radiation under anticyclonic conditions will be used to evaporate water which damps the temperature increase and may increase cloudiness, thus generating negative feedback loop. Between both,

it is a transition area where the regime will evolve from radiative limited (where high temperatures are more likely damped by water release from the soil) to soil-moisture limited (where high temperature are more likely enhanced by the positive feedback loop) in the course of the seasonal cycle. The transition timing will depend on latitude and year (more or less preceeding precipitation...). Figure 1 shows the spatial variability of soil moisture and shortwave surface net radiation and their evolution between May and June extracted from a simulation to evidence this transition from southern to northern Europe.

These processes are not the only ones that will determine temperature variability: the stability and the thermodynamical properties of the free troposphere can block these feedback loops by modifying the relative humidity of boundary layer top due to the air entrainement (Gentine et al. 2013; Stefanon et al., 2014). The modeling of such climate with accuracy is thus very difficult due to the possible rapid enhancement of initially small departures from observations by these positive and negative feedback loops. This explains why future projections are strongly related with the way models represent present-day variability (Boé and Terray, 2014).

However, model uncertainty is potentially reducible by using specific observations of the current climate because it helps identifying model errors. To evaluate models, previous studies mostly used gridded surface datasets for temperature and precipitation e.g E-OBS (Haylock et al., 2008), or satellite products such as Global Precipitation Climayology Project (Huffman et al., 1997) and sometimes other observations of cloudiness or/and radiative fluxes, e.g Chakroun et al. (under review), Tang et al., (2012) or Betts et al. (2007). This helped in pointing out the difficulties of climate models to reproduce present climate variability and possible sources of errors using correlations. But they did not allow to evaluate the full representation of water and energy cycles and complex interactions between large scale, clouds, land surface, boundary layer, and precipitation because of the different colocalisation, time and spatial resolutions of these climate time scales observations. Now, new long-term observational datasets including standard observations of pressure, temperature, humidity and precipitation colocalized with observations of clouds, surface and radiative fluxes emerge and allow to cross a new border in our understanding of such complex system. Among these datasets, the Canadian Paririe data used by Betts et al. (2014; 2015) really improved the knowledge in the land-surface-cloud-atmosphere coupling over northern part of North America thanks to the use of synergy of observations. However, the sensitivity of climate variability to the different components of this complex coupling depends on the

studied area: for instance, according to the study of Van den Hurk et al. (2012), Europe is less sensible than the United States to soil moisture.

Recently, efforts have been made to create the SIRTA-ReOBS dataset (Cheruy et al., 2013; Chiriaco et al., 2014), which is a reanalysis of observations collected since 2003 at SIRTA (Site Instrumental de Recherche en Télédetection Active; Haeffelin et al., 2005), a site located at about 20 km southwestern of Paris, France (Fig. 1). It includes standard observations, remote-sensing observations of clouds, aerosols, radiative and surface fluxes among others. The aim of this study is to evaluate one simulation performed in the framework of the HYdrological cycle in Mediterranean EXperiment (HyMeX; Drobinski et al., 2014) and the MED-CORDEX (COordinated Regional climate Downscaling EXperiment; Giorgi et al. 2009. MED-CORDEX is the Mediterranean focus of CORDEX; Ruti et al., 2015) programs against high quality data of SIRTA-ReOBS. It is a first step to improve the ability of models to reproduce temperature variability over the european transitional climatic area discussed above where the spread of models is generally strong (Boé and Terray, 2014), even if this step is just dedicated to one model at one site. However, this site is of particularly interest since it is located in the suburbs of Paris, an area concentrating several million of inhabitants and lots of human activity, thus very vulnerable to climate variability.

The next section describes the different datasets used in this study, namely SIRTA-ReOBS and the HyMeX/MED-CORDEX simulations, and the way we compare them. Section 3 deals with the seasonal cycle of temperature which presents a strong bias in summer. The sensitivity of this bias to water availability and clouds is investigated. Section 4 discusses the temperature variability at interannual time scales and focusses on the control of clouds and evaporation during summertime. Section 5 concludes and proposes some perspectives to this work.

2. Datasets

2.1 SIRTA reanalysis: SIRTA-ReOBS

This study is mainly based on observations collected at the SIRTA atmospheric observatory, located 20-km South West of Paris (2.2°E/48.7°N – 160 m of altitude; red star on Fig.1), from 2003 to 2013 (Haeffelin et al., 2005). This observatory has collected many observations, which are now synthesized into the so-called “SIRTA Re-OBS dataset” as described in

Cheruy et al. (2013) and Chiriaco et al., (2014). After many steps of data quality control and harmonization, the "SIRTA Re-OBS" file contains hourly averages of more than 40 variables at this site. The availability of the variables used in this study is shown in Figure 2. Most of the data used here are well sampled over the period of the study, excepted for the latent heat flux and the lidar profiles so caution is necessary to interpret results using them.

The lidar profiles allow defining cloud products based on Scattering Ratio (SR) values, which highlight the contribution of particles to the lidar signal (Annex 1, eq3). SR (z) is equal to 1 in absence of clouds and aerosols. Cloud detection for each profile and at each vertical layer is based on the SR thresholds that have been used in Chepfer et al. (2008, 2010) as following: $0.01 < SR(z) \leq 1$ clear, $1.2 < SR(z) < 5$ unclassified (existence of particles, could be optically thin clouds or aerosols). The threshold of cloud detection without ambiguity is set to 5 ($SR(z) \geq 5$). When the lidar signal is fully attenuated by optically thick clouds, the layers above are obscured and the SR values are very low. Hence a ground-based lidar is better suited to evaluate low clouds occurrence than high clouds.

By comparing SIRTA's meteorological data with Meteo-France operational ground stations selected for their potential influence on spatial averages within the grid mesh of their model containing the SIRTA site, Cheruy et al. (2013) showed that monthly means of relative humidity and surface temperature at SIRTA were always between the minimum and maximum values observed around. Differences between min and max can reach 10% for relative humidity and 2°C for temperature (even more during the heatwave of 2003) but the covered area is much larger than the size of the grid cell of the simulation used in this study. Champollion et al. (2009) compared observed data at urban and rural sites in May-June 2004 over this same area and showed that the nighttime temperature difference can reach several degrees while the daytime temperature is quite similar. For specific humidity, the diurnal cycle is more complex but the difference is less than 1g kg^{-1}. Thus, we should keep in mind that the amplitude of the model biases could be different using another surface station but the biases can not be attributed to a specific effect of the SIRTA site.

2.2 HyMeX/MED-CORDEX simulations

Two 20-year simulations were performed over the Mediterranean basin in the framework of MED-CORDEX (Giorgi et al. 2009; Ruti et al., 2015) and the HyMeX programs (Drobinski et al., 2014). These simulations perform a dynamical downscaling of the ERA-interim data (Simons et al. 2007) at 20 km horizontal resolution over the domain shown on Fig.1.

Indiscriminate nudging towards ERA-interim reanalysis is used to constrain the fields above the planetary boundary layer with a coefficient of $5x10^{-5}$ s^{-1} for temperature, humidity and velocity components. This reduces the internal variability of the different simulations and allows us to consider that the differences come mostly from the distinct forcings at the surface (Salameh et al., 2010; Omrani et al., 2013, 2015). Both simulations use the same set of parameterizations, except for the surface scheme. This set of parameterizations includes the Single-Moment 5-class microphysical scheme (Hong et al. 2004), the new Kain-Fritsch convection scheme (Kain 2004), the Yonsei University (YSU) planetary boundary layer (PBL) scheme (Noh et al. 2003) and a parameterization based on the similarity theory (Monin and Obukhov 1954) for the turbulent fluxes. The radiative scheme is based on the Rapid Radiative Transfer Model (RRTM) (Mlawer et al. 1997) and the Dudhia (1989) parameterization for the longwaves and shortwaves radiation, respectively. The lower boundary conditions of WRF are provided by two different land-surface schemes. In CTRL, soil moisture can evolve freely by using the sophisticated Rapid Update Cycle land-surface model (RUC: *Smirnova et al*., 1997 and 2000). In the second simulation, called SURF, the soil moisture availability is prescribed and set to climatological wintertime value preventing any soil moisture deficit condition. This simulation is also at 20 km and was not performed specifically for this study (otherwise we would have applied a seasonal cycle of soil moisture) but helps in interpreting the impact of surface on the results. This sensitivity simulation SURF covers the period January 1989- December 2008, while the CTRL simulation ends in November 2011. Outputs are available every 3 hours. In the following, the CTRL simulation is used by default as it is physically more realistic and covers a longer period. These companion simulations have already been used to understand the impact of soil moisture-atmosphere feedbacks on heat waves over France (Stefanon et al., 2014).

Since the horizontal resolution of the simulations is 20 km, we can wonder how much the previous results can be affected by the extraction of model data at the closest grid point of SIRTA coordinates. A comparison between the values at the SIRTA grid point and the grid points around (not shown) suggested that the spatial variability in the model impacts the seasonal cycle of temperature by about 0.5°, with urban grid points being warmer during nighttime in summer, in agreement with observations (Champollion et al., 2009). However, this difference between the grid points is small in comparison with the observed variability at different local stations over this area (Cheruy et al., 2013) and we conclude that using a more complex interpolation procedure than just extracting model data at the closest grid point would not modify the results. Note that the simulation doesn't use a urban module but the soil

type of Paris and near suburbs grid points correspond to urban area (less evapotranspiration). However, the difference that can be linked to heat storage in urban areas during winter is not taken into account.

2.3 Lidar simulator and computation of cloud occurrence

To compare consistently the clouds observed by the 532-nm lidar and those simulated by the model, we used a lidar simulator as done in Chiriaco et al. (2006). For this, we have adapted the COSP lidar simulator (Chepfer et al., 2008; 2010) to the WSM5 microphysics parameterization (Hong and Lim, 2006) used in these simulations, and to a ground based lidar (instead of spaceborne lidar). We first vertically interpolated the profiles of cloud properties over a common vertical grid and we computed the vertical profiles of the Scattering Ratio (SR) using the lidar equation (see Annex 1). The properties (size distribution and effective radius) of particles needed to compute SR are not direct diagnostics of the model and are obtained by using the same equations and hypotheses than those used in the WSM5 scheme.

SIRTA-ReOBS provides a distribution of SR values observed by the lidar for each hour with available data. Using these SR distributions every 3 hours(to be consistent with simulation), we've computed the seasonal cycle of the vertical profile of cloud occurrence as the number of SR values greater than 5 at each level over the number of SR values greater than 0.01 at the correponding level (i.e only the profiles that are not fully attenuated). For the simulation we have one instantaneous vertical profile of SR every 3 hours, and we use the same diagnostic for cloud occurrence.

To go further in details and provide detailed vertical information on cloud optical and physical properties, SR histograms can be built following Chepfer et al. (2010). For each level, and each SR bin (14 bins between 0.01 and >80), we compute the number of SR values which fall into the bin over the total number of SR values >= 0.01 (we still only consider the profiles that are not fully attenuated). The sum of all bins at each level is then equal to 1. It is represented in log for better readibility.

2.4 Monthly mean datasets.

To compare CTRL simulation with SIRTA-ReOBS, we computed the different monthly mean values over exactly the same days and hours, i.e for all 3-hr time steps between 1st January 2003 to 30th of November 2011 but when an observed data is lacking for a time step, we remove the corresponding simulated data before averaging. This first dataset is called d1. Note that the number of time steps taken into account depends on the parameters (see Fig.2).

However, except for lidar data for which a large part of missing data is due to a weather situation (no observations when precipitation occur), this study shows that missing data do not influence that much the results (at the scales considered here).

To compare the different simulations, we also defined two other datasets by reducing the period from 1st of January 2003 to 31st of December, 2008: one (hereafter called d2) in which all 3-hr time steps are considered, that is used to compare CTRL with SURF; the other one in which the time steps without observations are removed (hereafter called d3).

A last dataset (d4) is used that covers the longer period 2003-2011 with all 3-hr time steps. Table 1 summarizes the available datasets.

3. Seasonal cycle: a positive feedback enhancing summertime temperature bias?

3.1 Seasonal cycle of surface atmospheric parameters.

We used the SIRTA-ReOBS dataset to evaluate the seasonal cycle of several parameters in CTRL simulation. Figure 3 clearly indicates an overestimate of 2m-temperature (tas) during summertime which reaches 2-3°C while wintertime tas is quite well simulated. This summertime overestimate of surface temperature is consistent with a bad partitioning between sensible and latent heat fluxes and an underestimation of evaporative fraction (EF), as already demonstrated for CMIP5 models over mid-latitudes (Cheruy et al., 2013; 2014). Indeed, we compared the sensible and latent heat fluxes (hfss and hfls respectively) over the available period of these parameters (i.e few for latent heat flux but CTRLd1 and CTRLd2 remain quite similar) (Fig.3e et f). We can see that the simulated sensible heat flux (solid red line) is significantly too strong from spring to fall, while latent heat flux is strongly underestimated. However, compared to the values of heat fluxes averaged over Europe and presented in Stegehuis et al. (2012), the latent heat flux at SIRTA seems stronger than elsewhere, while the sensible heat flux is only slightly weaker than the averaged surrounding fluxes. It is likely due to the fact that the soil type at SIRTA is specific and not represented in the model, thus partly explaining the difference of latent heat flux, but not all. Note also that the maximum value of the latent heat flux appears earlier in the simulation (around May) than in observations (June, in agreement with the averaged fluxes over Europe), decreasing the EF value and reaching a soil-moisture limited regime starting in spring (EF < ~30%). Since there are only few data of heat flux, another way to check how much surface fluxes may impact the boundary layer (PBL) characteristics is to plot the seasonal and diurnal cycles of the relationship between tas and humidity at 2 m (huss). We can see on Fig. 4 that the observations show more or less a

linear relationship between tas and huss whatever the season and the time of the day, indicating radiation control of surface fluxes. On the contrary, the simulated relationship indicates a soil-moisture limited regime, since the moisture feeding of PBL is not sufficient in spring and summer during the afternoon, due to weaker latent heat flux, probably due to a lack of moisture availability into the soil. It generates warmer and drier low layers during daytime in spring and summer (Fig.4) and deeper PBL (not shown because this parameter has not yet been reanalysed over this period). The underestimate of precipitation amount in summer (Fig.3b) amplifies the soil dryness and the increase of sensible heat flux but the soil moisture deficit can also be explained by larger incoming solar radiation (Fig. 3c).

The overestimate of downwards shortwave flux at surface (SW) (about 60 W m^{-2}, Fig. 3c) is also consistent with the summertime overestimate of temperature. Several studies using WRF over the United States have pointed out this overestimate of SW (e.g Otte et al., 2012; Herwehe et al. 2014) but the consequence was an overestimate of summertime (convective) precipitation due to excess of latent heat flux. Katraglou et al. (2015) also pointed out a positive bias of shortwave radiation in summer over southern Europe using WRF, and suggest that this is induced by Kain-Fristch and Betts-Miller-Janjic convective schemes. Note that downwards longwave flux is slightly underestimated but with a nearly constant bias during the whole year (Fig.3d) so the reasons of the bias are likely not related.

To determine if this overestimate of SW is due to inaccurate radiative impacts of clouds or also by a lack of clouds, we use the lidar data and compare observed (OBSd3) and simulated (CTRLd3) cloud occurrences as explained in section 2.3. Fig. 5a and b show that non-precipitating low clouds are missing in the simulation in spring and summer, which is consistent with the overestimate of SW. To go further in details and have an idea about the physical properties of the missing clouds, SR histograms are built (see section 2.3). The comparison of SR histograms (Fig.6) shows that while lidar observations suggest that there are only small differences between winter and summer for non-precipitating clouds (the lidar is switched off when it rains), except they occur at lower levels in winter, the CTRL simulation indicates a strong seasonal cycle of low clouds with a nearly total absence of low clouds of weak SR values during summertime. It means that only the optically thick low clouds (SR>=40) are simulated by the model, while observations show a high number of optically thin low clouds (5<SR<20) in summer. These clouds mainly correspond to fair weather cumulus (Chepfer et al., 2013). Note that very thick clouds (SR>=80) are also missing in the simulation.

Hence CTRL simulation suggests the existence of a positive feedback: from spring, the soil dryness induces too weak evaporation fraction, that generates warmer, drier (and likely deeper) PBL during early summer. These conditions are not favorable to low clouds formation, increasing the shortwave surface fluxes arriving at surface and hence enhancing surface fluxes: the available soil moisture is then quickly evaporated (earlier than observations), favoring drier and drier soil in summer and high sensible heat flux, increasing again favorable conditions to warming. This hypothesis is consistent with previous studies (e.g Cheruy et al., 2013; 2014; Fischer et al., 2012).

3.2 Impact of water avaibility: importance of diurnal cycle

To better understand the origin of biases and test the impact of water avaibility on the CTRL biases, we use the SURF simulation in which soil moisture is always available. We used dataset d2 to compare SURFd2 with CTRLd2 since SURF is not available with dataset d1 (see Tab.1). The seasonal cycle of each parameter is represented by dashed blue line in Fig. 3. As shown by this figure, CTRLd1 and CTRLd2 present very similar seasonal cycles, which implies that i) missing data in observations do not influence the results that much in that case; ii) we can directly compare SURFd2 and CTRLd2 with OBSd1.

We can see that when soil moisture is available (SURF), the evaporation fraction increases (sensible heat flux (Fig.3e) is reduced to become comparable with observations, and the latent heat flux (Fig.3f) is increased, still not enough comparing to observations, but significantly). The maximum of latent heat flux occurs in July, as in the observations, meaning that the regime becomes radiative limited, and the surface temperature is strongly decreased. The air mass becomes even colder than observations in summer. Figure 4 shows that the boundary layer also becomes wetter than observations, which can explain the weaker latent heat flux since it is related to the humidity gradient between the surface and the lower atmosphere. Such impact of soil moisture on seasonal temperature, also presented in Stefanon et al. (2014) with the same simulations for heat waves, is in agreement with Van den Hurk et al. (2012).

However, the monthly means of radiative fluxes are not modified significantly in summer (they are slightly reduced in fall) in SURFd2, as already shown by Stefanon et al. (2014). In terms of clouds, Figures 5b and c show light differences between CTRLd3 and SURFd3 in summer with a bit more very low clouds in summer in SURFd3 and less clouds around 5 km, and more pronounced differences in fall at low levels. Figure 6f confirms the existence of very low clouds of moderate ($20<SR<30$) and strong SR ($SR>60$) in SURFd3 but the

difference is not important. The number of attenuated profiles at low levels is also enhanced in SURFd3 (not shown). To better compare the two simulations with the same number of profiles, we thus computed the vertical profiles of cloud occurrence without the lidar simulator (i.e from the condensed water mixing ratio) focusing in summer (JJA) using CTRLd2 and SURFd2 (i.e also including nighttime time steps and precipitating days). The interannual variability is shown in Fig.7a and b and reveals a significant modification of the vertical distribution of clouds below 8 km in summer between the two simulations, more pronounced than when using dataset d3 which is reduced to non-precipitating days and daytime and when using the lidar simulator because of the problem of fully attenuated profiles. We can thus wonder why these differences do not affect the monthly mean of shortwave radiative fluxes.

By considering the diurnal cycle of the differences between the two simulations, we can see that most low clouds in SURFd2 appear during nightime and early morning (fog-like) (Fig.7c and d), generating a decrease of SW in the morning in comparison with CTRLd2 (Fig.7e). This decrease of SW in the morning is almost compensated by an increase in the afternoon due to a difference of cloud occurrence in early afternoon at about 5 km (Fig.7c and d). This can be explained by the atmospheric stability: despite greater relative humidity at surface, the influence of important soil moisture can lead to unfavorable conditions to cloud formation in the afternoon, depending on the large scale conditions that prevail (Boe et al., 2013) and the thermodynamic conditions of free tropospheric air which is entrained into the boundary layer (Gentine et al., 2013). Stefanon et al. (2014) have shown that during heat waves, in the SURF simulation, the probability that the PBL is higher than the level of free convection (LFC) at 1500 UTC is zero over France, except over the Alps. We have checked that in general, during daytime, the atmospheric stability is smaller in CTRL than in SURF over this site in summer. Indeed, following the work of Boé et al. (2003) who have shown the strong link between the Total Totals Index (TTI) and precipitation over France, we used this index to test the stability of atmosphere. It is defined by:

$$TTI = Td850 - Ta500 + Ta850 - Ta500$$

where Ta850 (Ta500) is the atmopsheric temperature at 850 (500) hPa, Td850 is the dew point temperature at 850 hPa, and Ta850-Ta500 is the Vertical Totals Index and Td850-Ta500 is the Cross Totals Index. Higher the TTI, smaller the stability of the atmosphere. We have computed the mean values and standard deviation of TTI over 2003-2008 during JJA. Table 2 shows that SURF has lower mean value of TTI, and also higher occurrence of values under 40 which corresponds to very low likely convection.

However, both simulations have difficulties to simulate the non-precipitating clouds. It is possible that the set of parameterizations which is common to the two simulations produces inaccurate eddy diffusivity profiles thus preventing the boundary layer cumuli to form. Microphysics processes can also be involved through the production of raindrops and the surface scheme in the redistribution of energy and moisture. Testing other sets of parameterisation may improve the results as already shown by several authors (e.g Guttler et al., 2013; Garcia-Diez et al., 2012; Jousse et al., 2015). It will be done in a future work.

So, the surface temperature bias is strongly related to the surface regime (soil-moisture or radiative limited). The RUC soil scheme associated with these boundary layer (YSU) and convective (KF) parameterizations presents an unbalanced hydrological cycle that is returning moisture from land to the atmosphere too quickly, favoring the switch from radiative to soil-moisture regime too early in the seasonal cycle. We saw that wet soil strongly impacts the mean surface temperature. However it does not impact much the monthly mean values of shortwave radiative fluxes but modifies both the vertical distribution of clouds and their diurnal cycle. The year-to-year differences between wet and dry soils are also important as shown by Fig.7a and b. In the next section, despite the strong summer bias, we investigate the relative role of clouds and surface fluxes on the variability of temperature, at interannual and daily time scales, mainly focusing on summer.

4. Temperature variability: impact of large-scale dynamics, evaporation and clouds

4.1 Interannual variability of local temperature and extremes

It is of high importance to evaluate both the ability of the model to represent the temperature variability at present-day and the influences explaining this variability since several studies argue that the climate change signals will depend on the quality of present-day representation (Boé and Terray, 2014; Fischer et al., 2012).

Figure 8 shows that the interannual variability of monthly mean temperature is very well captured by CTRL simulation for all months, even during summertime despite the bias. We also plotted the monthly mean temperature of the reanalysis ERA-interim which nudges the CTRL simulation, except within the boundary layer. The fact that CTRL simulation and ERA-interim perform very well confirms that at this scale and this location, the variability of

monthly means is mainly controled by the influence of synoptic circulation, as already suggested by Cattiaux et al. (2011).

The interquartile range (IQR) (between the 25% and 75% quantiles of all mean daily temperature of each month) is considered to quantify the variability. It is represented by dashed lines on each suplot of Fig.8. It shows that the distribution of mean daily temperature is predicted with high accuracy by CTRL, even in summer. As analysed in CRU data by Lenderink et al. (2007) over the period 1961-1990, IQR is higher in June and July than in August, and values of IQR are similar despite the different period of analysis. Such good accurary of IQR by the simulation was not completely expected due to the biases discussed in previous section and the fact that the european climate is strongly dependent on the water and energy budgets (e.g Lenderink et al., 2007; Fisher et al., 2012; Vidale et al., 2007). Different aspects can explain this: i) the western location of this site where the large-scale dynamics strongly influence the interannual variability and modulate the land-surface-cloud-atmosphere feedbacks at interannual time scale (Boe et al., 2013); ii) the fact that neither observations, neither CTRL simulation are in an intermediate state concerning evaporation fraction: the strong soil moisture depletion for all the considered summers in CTRL leads to small year to year variations in evaporative fraction while in the observations, the soil stays wet most of the time due to specific soil conditions. This leads to the same weak variability. It does not mean that surface state does not influence the interannual variability, but its influence is reduced compared to other sites/other models.

However, when considering the maximum and minimum values for each year/each month, some discrepancies appear (dash-dotted lines on Fig.8), suggesting that at shorter time scales and for extreme events, the influence of clouds and evaporative fraction becomes more important.

4.2 Control of surface parameters by radiation and evaporation in summer (MJJAS)

4.2.1 Relationship between temperature and shortwave net radiation and evaporation.

To analyse how much the summer temperature is influenced by radiative and surface fluxes, we sorted the daily maximum values of temperature from May to September (Fig.9a) and used it as sorting criterion for evaporation and daily mean of net shortwave radiation (SWnet) (Figs.9b and c respectively). We also did it for each month separatly but results are similar in

472 average, except that in August, evaporation is lower thus reducing the variability of
473 temperature. Several datasets are used (see Table 1): dataset d1 for temperature and radiative
474 fluxes; and dataset d4 (model only) for evaporation. Figure 10a compares the annual
475 distribution of the daily observed and simulated SWnet and shows that the spread of values is
476 important in summer, and that simulated values are in the range of observed ones except that
477 very low values of SWnet during summer are missing, in agreement with the lack of clouds
478 discussed in previous section.
479 Figure 9a shows the quantile plots of sorted maximum temperature. Datasets d1 and d3 (see
480 legend on Figure for details) are plotted so that the sensitivity of the results to the length of
481 the datasets can be assessed but the conclusion is that results are not that much affected by the
482 lack of data. This figure shows that: i) CTRL simulation does not tend to overestimate
483 extreme values more than median values since the slopes of evolution of T from the 5^{th}
484 quantile up to the 95^{th} quantile are similar; ii) the slopes in SURF are weaker than for OBS
485 and CTRL, showing similar values than OBS for the lower quantiles and lower values for
486 higher quantiles. This can be explained by the influence of evaporation: indeed, the
487 relationship between temperature and evaporation (Fig.9b) shows nearly constant values of
488 evaporation for CTRL whatever the temperature quantile, while in SURF, evaporation
489 increases with temperature quantiles. As explained by Stefanon et al. (2012), the more intense
490 evaporation damps the warmer temperature and then reduces the temperature variability and
491 the maximum values of temperature. The soil moisture availability in SURF thus strongly
492 contributes to reduce the slope on Fig.10a. In CTRL, the values of evaporation are too weak
493 to exert a control on temperature variability at this daily scale. This suggests a dominant effect
494 of shortwave radiation on the day-to-day temperature variability in CTRL simulation.
495
496 When considering the influence of shortwave (Fig. 10c), CTRL shows a linear relationship
497 between SW and daily maximum temperature quantile up to the 75^{th} quantile, with a
498 difference of about 100 W m^{-2} between the value at the 75^{th} quantile and the one at the 5^{th}
499 quantile (hereafter called ΔSW). In SURF, SW goes on increasing at the higher temperatures.
500 Stronger SW favors stronger evaporation when soil moisture is available and thus explains the
501 evaporation-temperature relationship in SURF. The observations present a weaker ΔSW,
502 close to zero, indicating that the short wave radiation contributes stronger to the day-to-day
503 temperature variability in the model. In the model, for quantiles up to the 75^{th} one, the
504 temperature is controlled by the synoptic situation that prevails and which induces strong
505 variations of SW depending on the dominant cloud cover. For the higher temperatures, the

averaged value of SW stays the same. The temperature of the day will then likely depend on the variability of SW within a bin (due to the cloud cover) and the heat storage in the boundary layer during the preceeding days (Miralles et al., 2014).

4.2.2 Role of clouds on temperature variability and bias

The shortwave downwards and net radiations depend on the presence, altitude, optical thickness and properties of clouds and on the solar zenith angle and surface albedo. To better consider the role of clouds and to reduce the effect of the change in solar zenith angle between May and end of September, we thus use the effective cloud albedo (α_{cloud}) as defined by Betts (2007):

$$\alpha_{cloud} = -SWCRE/SW_{clear}$$

where

$$SWCRE = SW-SW_{clear}$$

is the cloud radiative effect (CRE) on shortwave. The effective cloud albedo represents the fraction of the clear sky flux reflected by the cloud field. Figure 10 shows a comparison between the observed short-wave fluxes, cloud radiative effect and cloud albedo and the simulated ones in CTRLd1.

The absence of low clouds (Figs.5 and 6) induces an underestimate of cloud radiative effect (cloud albedo), as shown by Figs.10b and c. Indeed, Figure 10c shows the seasonal cycle of α_{cloud} from monthly means at 12 UTC and its interannual variability. It shows that the bias between CTRL (red) and OBS (black) is significant, especially in summer, although the spread of daily values is important (Fig.10b). The black and red dashed lines which represent the monthly means of the surface albedo for observations and simulation respectively, indicate that despite the resolution of the model and the fact we compare at one single site, the surface albedo is very well simulated in average and can not explain differences in net fluxes. The cloud albedo bias is partly due to an underestimate of strong negative values of SWCRE (Fig.10b) but all categories of clouds contribute to this underestimate as indicated by Fig.10d. Indeed, for all values of simulated α_{cloud} except very opaque simulated clouds, most values are negatively biased. Figure 10f indicates that while the number of α_{cloud} values in summer shows a decreasing linear trend from 20% of values for the first bin (α_{cloud} <0.1) to 0% for the last bin (α_{cloud}=1) in observations, more than 50% of simulated α_{cloud} values correspond to very low values (<0.1). It confirms what has been analysed with the lidar (Fig.6). Note that the linear trend for the other bins is quite similar. In winter (Fig.10e), the distribution is

different with a peak at 0.7-0.8, which is represented by the model, although a little bit underestimated (also note the higher number of low values as in summer).

Following Betts' methodology (e.g. Betts et al., 2006; Betts, 2009), Figure 11a stratifies temperature anomaly in summer (MJJAS) by cloud albedo. Temperature anomaly is chosen here instead of temperature since we are interested in the effect of clouds on the temperature variability. Temperature anomaly is computed as the difference between the temperature of the day and the average temperature of this julian day over the 9 years (2003-2011) and then stratified by α_{cloud} with 50 samples in each bin.

Figure 11a confirms that while the amplitude of seasonal cycle of temperature is dominated by surface fluxes (Fig.3), the cloud cover influences the surface temperature variability. It is in agreement with Fig. 9c, but, by using effective cloud albedo instead of SWnet and temperature anomaly instead of temperature quantile, it removes the effect of seasonal cycle of SWnet that likely contributes to the relationship in Fig.9c. It thus allows to detect finer scale of variability. In average, the stronger the cloud albedo is, the stronger the cooling is important in summer, but the dispersion is important, even more for values of α_{cloud} less than 0.5. Most cloudy free days ($\alpha_{cloud} < 0.1$) correspond to a positive anomaly of temperature, while about 70% of anomalies are negative for $\alpha_{cloud} > 0.5$. The model tends to underestimate the effect of warming of clouds of weak albedo ($\alpha_{cloud} <0.3$), as shown by Fig.11b. The effect of clouds on temperature variability is modified over wet soils as shown by Fig. 11b: SURF underestimates warming of optically thin clouds more than CTRL (warmer temperature are damped by evaporation) and overestimates cooling of clouds more than CTRL (more fog in the morning). The interpretation of Figs.9c and 11a, b is that in observations, clouds often exist whatever the synoptic situation, which induces the same average values of SW in each bin of temperature (mainly driven by synoptic situation as shown previously). However, inside a bin, the variability of SW values is high and days without clouds tends to enhance the maximum temperature. On the contrary, in the model, fair weather low clouds are not simulated, and then, high temperature are associated with high SW values with lower variability inside each bin. Positive temperature anomalies associated with absence of clouds is then not enhanced (Fig.11b).

The daytime precipitation (between 09 and 18 UTC) stratified by cloud albedo (Fig.11c) shows that the probability of occurrence of rain increases for cloud albedo greater than 0.4 for simulations and observations but the mean rain rate does not significantly increase, except in OBS for the highest values of cloud albedo (Fig. 11d). Higher than 0.4, the probability of rain increases a bit more quickly for SURF and CTRL than for OBS. The occurrence reaches 50%

for simulations while only 35% in observations for opaque clouds. However, Fig.11d shows that it rains very lightly in SURF during daytime (even the 80^{th} percentile is around 1 mm/3hr). CTRL and OBS have similar values of rain rate for median (around 1 mm/3hr) and even up to 80^{th} percentile (around 2-3 mm/3hr, except for the highest values of cloud albedo which reach 5 mm/3hr in OBS), but extreme values (95^{th} percentile) are significanty stronger in OBS than CTRL (reaching 20 mm/3hr in OBS and less than 10 in CTRL; not shown), which is expected when comparing a local rain rate with a 20x20 km^2 grid cell (Chen and Knutson, 2008).

5. Conclusion

The objective of this paper is to understand how cloud cover and surface fluxes control the temperature variability over the SIRTA site and in the model. This is of particular importance since this site is located in a climatic transitional area where models usually show strong dispersions. A schematic diagram showing the temperature range of observations and simulations as a function of surface conditions and surface net radiation summarizes the study (Fig.12). The main results of the study are:

- The large scale conditions have a strong impact on the interannual variability of temperature: this can be explained by the north-western location of the site, thus directly under the influence of air masses from the Atlantic. It is likely that this control is reduced over Central Europe.
- The soil moisture exerts a strong control on the seasonal cycle of the temperature. The transition from radiation to soil moisture limited regime that occurs earlier in simulations than in observations leads to an overestimate of summertime temperature in CTRL simulation. Bullock (2014) already observed this unbalanced hydrological cycle with NOAH surface scheme. The role of the surface scheme is not demonstrated here. Indeed, the soil dryness is associated with an overestimate of shortwave radiation. Consequently, the soil dryness can be attributed either to the excessive energy arriving at surface or to an unbalanced hydrologycal cycle or both. The overestimate of SW is consistent with a lack of low clouds in the simulation. However, it couldn't be demonstrated the feedback between the dryness of the soil and the lack of low clouds. Indeed, a wetter soil produces colder and wetter low atmospheric layers but also more stable atmosphere during daytime preventing the formation of low clouds. We would need to test other set of parameterizations to

improve our understanding of the model behavior and test what happens when the radiative limited regime dominates until July and when clouds exist. This work is underway. Also, Herwehe et al. (2014) and Alapaty et al. (2012) demonstrated that introducing subgrid-scale cloud-radiation feedbacks in regional climate simulations significantly decreases the summertime overestimate of SW. It is not sure that the absence of subgrid scale cloud-radiation feedbacks plays such important role in our simulation since it seems that convective clouds are not so numerous in the simulation due to the too dry atmosphere but it will be investigated using WRF version 3.7 in the next future.

- At shorter time scales, the control of surface radiation becomes higher. In CTRL (dry soil and no clouds), higher temperatures are linearly associated with higher SW, the main driver being presence/absence of clouds depending on the synoptic situation. A wet soil (SURF) mitigates the effect of radiation due to modulation by evaporation. Observations show a stronger variability of cloud cover in summertime, and then a stronger impact of cloud cover on temperature variability within each range of temperature but no relationship between mean SW and temperature quantile. The effect of clouds on temperature variability in CTRL also exists, even if more lightly.
- Both in observations and simulations, clouds with albedo less than 0.4 are non-precipitating clouds and for higher albedo effects, occurrence of precipitation increases but not the average rain rate. However, clouds with very high albedo effects are particularly missing in simulations, generating lighter strong precipitation events.

In a future study, the quantification of warming by clouds will be adressed in more details. Other models participating to HyMeX/MED-CORDEX programs will also be evaluated against SIRTA-ReOBS to better explain the diagnosed spread. This study should be extended to other french sites which produce similar reanalysis of observations in a context of french and european concertations.

References:

Alapaty, K., Herwehe, J.A., Otte, T.L., Nolte, C.G., Bullock, O.R., Mallard, M.S., Kain, J.S. and Dudhia, J. (2012). Introducing subgrid-scale cloud feedbacks to radiation for regional meteorological and climate modeling. *Geophysical Research Letters 39: doi: 10.1029/2012GL054031. issn: 0094-8276.*

Betts A.K., 2009: Land surface atmosphere coupling in observations and models. *J. Adv. Model Earth Syst.*, 1, art#4, 18pp. doi:10.3894/JAMES.2009.1.4

Betts, A. K. (2007), Coupling of water vapor convergence, clouds, precipitation, and land-surface processes, J. Geophys. Res., 112, D10108, doi:10.1029/2006JD008191.

Betts, A.K., R. Desjardins, A.C.M. Beljaars and A. Tawfik (2015). Observational study of land-surface-cloud-atmosphere coupling on daily timescales. Front. Earth Sci. 3:13. doi: 10.3389/feart.2015.00013

Betts, A.K., R. Desjardins, D. Worth and B. Beckage (2014), Climate coupling between temperature, humidity, precipitation and cloud cover over the Canadian Prairies. J. Geophys. Res. Atmos., 119, 13305-13326, doi:10.1002/2014JD022511.

Boé J. and L. Terray, 2014: Land–sea contrast, soil-atmosphere and cloud-temperature interactions: interplays and roles in future summer European climate change. *Clim. Dyn.* **42**:683–699 DOI 10.1007/s00382-013-1868-8

Boé and Terray, 2008: Uncertainties in summer evapotranspiration changes over Europe and implications for regional climate change. *Geophysical Research Letters*, **35**, L05702, *doi:10.1029/2007GL032417*

Boé J., 2013: Modulation of soil moisture-precipitation interactions over France by large scale circulation. *Climate Dynamics*, **40**(3-4), 875-892

Bullock, O. R., Jr., K. Alapaty, J. A. Herwehe, M. S. Mallard, T. L. Otte, R. C. Gilliam, C. G. Nolte, 2014: An observation-based investigation of nudging in WRF for downscaling surface climate information to 12-km grid spacing. J. Appl. Meteor. Climatol., 53, 20-33.

Cattiaux, J., and P. Yiou (2012), Contribution of atmospheric circulation to remarkable European temperatures of 2011, in « Explaining Extreme Events of 2011 from a Climate Perspective », Bulletin of the American Meteorological Society, 93, 1041-1067. doi :10.1175/BAMSD-12-00021.1

Chakroun M., Bastin S., Chiriaco M., Chepfer H.: Characterization of vertical cloud variability over Europe using spatial lidar observations and regional simulation. Sub. to Clim. Dyn (special issue Med-Cordex).

671 Champollion C., Drobinski P., Haeffelin M., Bock O., Tarniewicz J., Bouin M.N.,
672 Vautard R., 2009: Water Vapor Variability Induced by Urban/Rural Heterogeneities during
673 Convective Conditions. *Quart. J. Roy. Meteorol. Soc.*, **135**, 1266-1276
674 Chen C.-T., and Knuston T., 2008: On the verification and comparison of extreme
675 rainfall indices from climate models. J. of Clim., **21**, 1605-1621.
676 Chepfer H., S. Bony, D. M. Winker, M. Chiriaco, J.-L. Dufresne, and G. Seze, 2008:
677 Use of CALIPSO lidar observations to evaluate the cloudiness simulated by a climate model.
678 *Geophys. Res. Lett.*, **35**, L20804, doi: 10.1029/2012GL053385.
679 Chepfer H., S.Bony, D. M. Winker, G. Cesana, JL. Dufresne, P. Minnis, C.J.
680 Stubenrauch, and S. Zeng, 2010: The GCM Oriented CALIPSO Cloud Product (CALIPSO-
681 GOCCP), *J.of Geophys. Res.*, **105**, D00H16, doi: 10.1029/2009JD012251.
682 Chepfer H., G. Cesana, D. Winker, B. Getzewich, M. Vaughan, And Z. Liu, 2013:
683 Comparison of Two Different Cloud Climatologies Derived from CALIOP-Attenuated
684 Backscattered Measurements (Level 1): The CALIPSO-ST and the CALIPSO-GOCCP.
685 *American Meteorological Society*, **30**, 725-744. DOI: 10.1175/JTECH-D-12-00057.1
686 Cheruy F., A. Campoy, J.-C. Dupont, A. Ducharne, F. Hourdin, M. Haeffelin, M.
687 Chiriaco, A. Idelkadi, 2013: Combined influence of atmospheric physics and soil hydrology
688 on the simulated meteorology at the SIRTA atmospheric observatory. *Clim. Dyn.* **40**, 2251–
689 2269, doi : 101007/s00382-012-1469-y
690 Cheruy F., J. L. Dufresne, F. Hourdin, and A. Ducharne, 2014: Role of clouds and
691 land-atmosphere coupling in midlatitude continental summer warm biases and climate change
692 amplification in CMIP5 simulations. Geophysical Research Letters, 41:6493-6500
693 Chiriaco M., R. Vautard, H. Chepfer, M. Haeffelin, J. Dudhia, Y. Wanherdrick, Y.
694 Morille and A. Protat, 2006: The ability of MM5 to simulate ice clouds: systematic
695 comparison between simulated and measured fluxes and lidar/radar profiles at the SIRTA
696 atmospheric observatory. *American Meteorological Society*, **134**, 897-918
697 Chiriaco M., S. Bastin, P. Yiou, M. Haeffelin, J.-C. Dupont, M. Stéfanon, 2014:
698 European heatwave in July 2006: observations and modeling showing how local processes
699 amplify conducive large-scale conditions, Geo. Res. Let., 41, 5644–5652,
700 doi:10.1002/2014GL060205
701 Dee D, Uppala S, Simmons A, Berrisford P, Poli P, Kobayashi S, Andrae U,
702 Balmaseda M, Balsamo G, Bauer P, Bechtold P, Beljaars A C M, van de Berg L, Bidlot J,
703 Bormann N., Delsol C, Dragani R, Fuentes M, Geer A J, Haimberger L, Healy S B, Hersbach
704 H, Hólm E V, Isaksen L, Kållberg P, Köhler M, Matricardi M, McNally A P, Monge-Sanz B

M, Morcrette J J, Park B K, Peubey C, de Rosnay P, Tavolato C, Thépaut J N and Vitart F 2011 The era-interim reanalysis: Configuration and performance of the data assimilation system. Q. J. R. Meteorol. Soc., 137, 553–97.

Della-Marta P. M., J. Luterbacher, H. von Weissenfluh, E. Xoplaki, M. Brunet, and H. Waner, 2007: Summer heat waves over western Europe 1880-2003, their relationship to large-scale forcings and predictability. *Clim. Dyn.*, **29**, 251 – 275.

Drobinski P., V. Ducrocq, P. Alpert, E. Anagnostou, K. Béranger, M. Borga, I. Braud, A. Chanzy, S. Davolio, G. Delrieu, C. Estournel, N. Filali Boubrahmi, J. Font, V. Grubišić, S. Gualdi, V. Homar, B. Ivančan-Picek, C. Kottmeier, V. Kotroni, K. Lagouvardos, P. Lionello, M. C. Llasat, W. Ludwig, C. Lutoff, A. Mariotti, E. Richard, R. Romero, R. Rotunno, O. Roussot, I. Ruin, S. Somot, I. Taupier-Letage, J. Tintore, R. Uijlenhoet, and H. Wernli, 2014: HyMeX: A 10-Year Multidisciplinary Program on the Mediterranean Water Cycle. *Bull. Amer. Meteor. Soc.*, **95**, 1063–1082. doi: http://dx.doi.org/10.1175/BAMS-D-12-00242.1

Dudhia J., 1989: Numerical Study of Convection Observed during the Winter Monsoon Experiment Using a Mesoscale Two-Dimensional Model. *J. Atmos. Sci.*, **46**, 3077–3107. doi: http://dx.doi.org/10.1175/1520-0469(1989)046<3077:NSOCOD>2.0.CO;2

Fink A.H. and co-authors, 2004: The 2003 European summer heatwaves and drought – synoptic diagnosis and impacts. *Weather*, **59**, 209–216.

Fischer, E.M. and C. Schär, 2010: Consistent geographical patterns of changes in high-impact European heatwaves. Nature Geoscience,

Fischer E. M., J. Rajczak, and C. Schär, 2012: Changes in European summer temperature variability revisited. *Geophys. Res. Lett.*, **39**, L19702.

Gao X., Pal J.S., Giorgi F., 2006: Projected changes in mean and extreme precipitation over the Mediterranean region from high resolution double nested RCM simulation. *Geophys. Res. Lett.*, **33**, L03706

García-Díez, M., J. Fernández, L. Fita, and C. Yagüe (2013), Seasonal dependence of WRF model biases and sensitivity to PBL schemes over Europe, Quart. J. Roy. Meteor. Soc., 139(671), 501-514,doi:10.1002/qj.1976

Gentine, P., A. A. M. Holtslag, F. D'Andrea, and M. Ek Surface and atmospheric controls on the onset of moist convection over land, J Hydrometeorol, 130211131121003, doi:10.1175/JHM-D-12-0137.1.

Giorgi F., Jones C., Asrar R. G., 2009: Addressing climate information needs at the regional level: the CORDEX framework, WMO Bulletin 58 (3) - July 2009, p183

738 Giorgi, F. (2006), Climate change hot-spots, Geophys. Res. Lett., 33, *L08707*,
739 *doi:*10.1029/2006GL025734.
740 Güttler I, Č Branković, TA O'Brien, E Coppola, B Grisogono, F Giorgi, 2014:
741 Sensitivity of the regional climate model RegCM4.2 to planetary boundary layer
742 parameterisation. Clim. Dyn., 43(7), 1753-1772
743 Haeffelin, M., L. Barthes, O. Bock, C. Boitel, S. Bony, D. Bouniol, H. Chepfer, M.
744 Chiriaco, J. Cuesta, J. Delano¨e, P. Drobinski, J.-L. Dufresne, C. Flamant, M. Grall, A.
745 Hodzic, F. Hourdin, F. Lapouge, Y. Lemaitre, A. Mathieu, Y. Morille, C. Naud, V. No¨el, B.
746 OHirok, J. Pelon, C. Pietras, A. Protat, B. Romand, G. Scialom, and R. Vautard, 2005:
747 SIRTA, a ground-based atmospheric observatory for cloud and aerosol research. *Annales*
748 *Geophysicae*, **23**, 253–275.
749 Hawkins E. and R. Stutton, 2009: The potential to narrow uncertainty in regional
750 climate predictions. *American Meteorological Society.*1095-1107
751 Haylock MR, Hofstra N, Klein Tank AMG, Klok EJ, Jones PD, NewM (2008) A
752 European daily high-resolution gridded data set of surface temperature and precipitation for
753 1950–2006. J Geophys Res 113:D20119
754 Herwehe, J. A., K. Alapaty, T. L. Spero, and C. G. Nolte, 2014: Increasing the
755 credibility of regional climate simulations by introducing subgrid-scale cloud-radiation
756 interactions. J. Geophys. Res. Atmos., 119, 5317–5330, doi:10.1002/2014JD021504.
757 Hong, S.Y., J. Dudhia, and S.H. Chen 2004: A revised approach to ice microphysical
758 processes for the bulk parameterization of clouds and precipitation, Mon. *Weather Rev*., **132**,
759 103–120.
760 Huffman, George J., Robert F. Adler, Philip Arkin, Alfred Chang, Ralph Ferraro,
761 Arnold Gruber, John Janowiak, Alan McNab, Bruno Rudolf, Udo Schneider, **1997**: The
762 Global Precipitation Climatology Project (GPCP) Combined Precipitation Dataset.
763 *Bulletin of the American Meteorological Society*: Vol. **78**, No. 1, pp. 5-20.
764 Ionita M, Lohmann G, Rimbu N, Scholz P (2012a) Dominant modes of Diurnal
765 Temperature Range variability over Europe and their relationships with large-scale
766 atmospheric circulation and sea surface temperature anomaly patterns. J Geophys Res. doi:10.
767 1029/2011JD01666
768 Ionita M, Lohmann G, Rimbu N, Chelcea S, Dima M (2012b) Inter-annual to decadal
769 summer drought variability over Europe and its relationship to global sea surface temperature.
770 Clim Dyn., 38(1–2):363–377

Ionita M., Boroneant C., Chelcea S., 2015: Seasonal modes of dryness and wetness variability over Europe and their connections with large-scale atmospheric circulation and global sea surface temperature. Clim. Dyn., DOI 10.1007/s00382-015-2508-2

Jousse A., Hall A., Sun F., Teixeira J., 2015: Causes of WRF surface energy fluxes biases in a stratocumuls region. Clim. Dyn., doi 10.1007/s00382-015-2599-9.

Kain J.S., 2004: The Kain–Fritsch Convective Parameterization: An Update. *Journal of Applied meteorology*, **43**, 170-181

Katragkou et al., 2015: Regional climate hindcast simulations within EURO-CORDEX: evaluation of a WRF multi-physics ensemble. *Geosci. Model. Dev.*, 8, 603-618.

Lenderink G., A. van Ulden, B. van den Hurk and E. van Meijgaard, 2007: Summertime inter-annual temperature variability in an ensemble of regional model simulations: analysis of the surface energy budget. *Clim. Change*. **81**: 1,233-274. DOI 10.1007/s10584-006-9229-9

Menut L., 2003, Adjoint modelling for atmospheric pollution processes sensitivity at regional scale during the ESQUIF IOP2, *Journal of Geophysical Research - Atmospheres*, 108, D17

Miralles, D. G., Teuling A. J., van Heerwaarden, C. C., de Arellano, J. V-G., 2014: Mega-heatwave temperatures due to combined soil desiccation and atmospheric heat accumulation. *Nature Geosci.* 7, 345–349.

Mlawer J. E., Taubma J. S., Brown D. P., Iancono M. J., Clough A. S., 1997: Radiative transfer for inhomogeneous atmospheres: RRTM, a validated correlated-k model for the longwave, *J. Geophys. Res*, **102**, Issue D14, 16663–16682, DOI: 10.1029/97JD00237

Monin A. S. and Obukhov, 1954: A. M. Basic laws of turbulent mixing in the surface layer of the atmosphere. Tr. Akad. Nauk SSSR Geophiz. Inst. **24**(151):163-187

Noh Y., W. G. Cheon and S. Y. Hong, 2003: Improvement of the k-profile model for the planetary boundary layer based on large eddy simulation data. *Boundary-layer meteorology*, **107**, 401-427

Nogaj M., P. Yiou, S. Parey, F. Malek, and P. Naveau, 2006: Amplitude and frequency of temperature extremes over the North Atlantic region. Geophys. Res. Let. , 33, issue 10, L10801, doi:10.1029/2005GL024251.

Omrani H, Drobinski P, Dubos T (2015) Using nudging to improve global-regional dynamic consistency in limited-area climate modeling: What should we nudge? Clim. Dyn. 44:1627--1644

Omrani H, Drobinski P, Dubos T (2013) Optimal nudging strategies in regional climate modelling: Investigation in a Big-Brother Experiment over the European and Mediterranean regions. Clim. Dyn. 41:2451--2470

Otte, T. L., C. G. Nolte, M. J. Otte, J. H. Bowden, 2012: Does nudging squelch the extremes in regional climate modeling? J. Climate, 25, 7046-7066.

Ruty P., Somot S., et al., 2015: Med-CORDEX initiative for Mediterranean climate studies. In revision *to BAMS*

Salameh T, Drobinski P, Dubos T. 2010. The effect of indiscriminate nudging time on large and small scales in regional climate modelling: Application to the Mediterranean basin. Q. J. R. Meteorol. Soc. 136: 170–182, doi:10.1002/qj.518.

Schär, C., P.L. Vidale, D. Lüthi, C. Frei, C. Häberli, M. Liniger and C. Appenzeller, 2004: The role of increasing temperature variability in European summer heat waves. *Nature,***427**, 332-336

Seneviratne, S.I.**,** T. Corti, E.L. Davin, M. Hirschi, E.B. Jaeger, I. Lehner, B. Orlowsky, and A.J. Teuling, 2010: Investigating soil moisture-climate interactions in a changing climate: A review. *Earth-Science Reviews,* 99, 3-4, 125-161, doi:10.1016/j.earscirev.2010.02.004.

Skamarock W. C. and J. B. Klemp, 2008: A time-split nonhydrostatic atmospheric model for weather research and forecasting applications. *Journal of Computational Physics* **227**:7, 3465-3485. Online publication date: 1-Mar-2008.

Smirnova T. G.**,** Brown John M.**,** B. Stanley G., 1997**:** Performance of Different Soil Model Configurations in Simulating Ground Surface Temperature and Surface Fluxes. *Mon. Wea. Rev.*, **125**, 1870–1884. doi: http://dx.doi.org/10.1175/1520-0493(1997)125<1870:PODSMC>2.0.CO;2

Smirnova, T. G., J. M. Brown, S. G. Benjamin, and D. Kim (2000), Parameterization of cold-season processes in the MAPS land-surface scheme, J. Geophys. Res., **105(D3)**, 4077–4086, doi:10.1029/1999JD901047.

Stefanon M., Drobinski P., D'Andrea F., Lebeaupin-Brossier C., Bastin S., 2014: Soil moisture-temperature feedbacks at meso-scale during summer heat waves over western Europe. Climate Dynamics, 42 (5-6), 1309-1324, DOI : 10.1007/s00382-013-1794-9.

Stéfanon, M., P. Drobinski, F. D'Andrea, *and* N. deNoblet-Ducoudré *(*2012*),* Effects of interactive vegetation phenology on the 2003 summer heat waves, J. Geophys. Res., 117, *D24103, doi:*10.1029/2012JD018187.

Stegehuis, A., R. Teuling, P. Ciais, R. Vautard and M. Jung, 2013b: Future European temperature change uncertainties reduced by using land heat flux observations. Geophys. Res. Letters, 40 (10), 2242-2245. DOI: 10.1002/grl.50404

Stegehuis, A., R. Vautard, P. Ciais, R Teuling, M. Jung, and P. Yiou, 2013a: Summer temperatures in Europe and land heat fluxes in observation-based data and regional climate model simulations. Climate Dynamics, 41, 455-477.

Tang Q., Guoyong Leng and Pavel Ya. Groisman, 2012: European Hot Summers Associated with a Reduction of Cloudiness. *J. Climate*, **25**, 3637–3644. doi: http://dx.doi.org/10.1175/JCLI-D-12-00040.1

Teuling, A. J., et al. (2009), A regional perspective on trends in continental evaporation, Geophys. Res. Lett., 36, L02404, doi:10.1029/2008GL036584

Van den Hurk B., Doblas-Reyes F., Balsamo G., Koster R.D., Seneviratne S.I. Camargo H. Jr, 2012: Soil moisture effects on seasonal temperature and precipitation forecast scores in Europe. Clim. Dyn., 38, 349-362.

Vautard R. and co-authors, 2007: Summertime European heat and drought waves induced by wintertime mediterranean rainfall deficit. *Geophys. Res. Lett.*, **34**, L07711

Vautard, R., Moran, M. D., Solazzo, E., Gilliam, R. C., Matthias, V., Bianconi, R., Chemel, C., Ferreira, J., Geyer, B., Hansen, A. B., Jericevic, A., Prank, M., Segers, A., Silver, J. D., Werhahn, J., Wolke, R., Rao, S. T., and S. Galmarini, 2012, Evaluation of the meteorological forcing used for the Air Quality Model Evaluation InternationaI Initiative (AQMEII) air quality simulations. Atmos. Environ., doi:10.1016/j.atmosenv.2011.10.065.

Vautard, R. and P. Yiou, 2009, Control of recent European surface climate change by atmospheric flow, *Geophys. Res. Lett.*, 36, L22702, 10.1029/2009GL040480

Vautard, R., A. Gobiet, D. Jacob, M. Belda, A. Colette, M. Déqué, J. Fernández, M. García-Díez, K. Goergen, I. Güttler, T. Halenka, T. Karakostas, E. Katragkou, K. Keuler, S. Kotlarski, S. Mayer, E. van Meijgaard, G. Nikulin, M. Patarčić, J. Scinocca, S. Sobolowski, M. Suklitsch, C. Teichmann, K. Warrach-Sagi, V. Wulfmeyer, P. Yiou, 2012 : The simulation of European heat waves from an ensemble of 1 regional climate models within the EURO-CORDEX project. Climate Dynamics, 41, 2555-2575.

Vidale P. L., D. Lüthi, R. Wegmann, C. Schär., 2007: European summer climate variability in a heterogeneous multi-model ensemble. Clim. Change, 81, 209-232. doi 10.1007/s10584-006-9218-z

Xoplaki E., J. F. Gonzalez-Rouco, J. Luterbacher and H. Wanner, 2004: Wet season Mediterranean precipitation variability: influence of large-scale dynamics and trends. *Clim. Dyn*. **23**: 63–78, DOI 10.1007/s00382-004-0422-0

period and frequency	2003-2011 observations sampling only	2003-2008 all days, every 3hr	2003-2008 observations sampling only	2003-2011 all days, every 3hr
OBS	OBSd1	-	OBSd3	
CTRL	CTRLd1	CTRLd2	CTRLd3	CTRLd4
SURF	-	SURFd2	SURFd3	

Table 1: list of datasets used.

	TTI mean value	TTI standard deviation	occurrence of values < 40
CTRL	43.5	2.3	35%
SURF	41.6	2.7	57%

Table 2: Total Totals Index (TTI) mean value and standard deviation for CTRL and SURF simulations. The last column indicates the percentage of values under the threshold of 40.

881
882 List of Figures:
883
884 Fig.1 Domain of the simulation and location of SIRTA site (red star). Colormap presents
885 a) the soil moisture of May averaged over 2000-2009; (b) same as a) for June; c) the
886 shortwave surface net radiation of May averaged over 2000-2009; d) same as c) for
887 June.
888
889 **Fig.2** Observations availability: Blue histograms indicate the number of days with
890 measurements (the maximum being 3256 over the period of the study) for each
891 parameter. Red bars indicate the average number of hours per day with measurements
892 (only considering 0, 3, 6, 9, 12, 15, 18 and 21 UTC). rlds stands for 'radiative longwave
893 downwards at surface', rlus is the same but upwards, rsds and rsus are the same for
894 shortwave and rsdscs/rldscs are for clear sky fluxes. tas is for temperature at 2-m. hurs
895 and huss are respectively relative and specific humidity at 2-m, pr is for precipitation,
896 hfss and hfls are for sensible and latent heat fluxes respectively. SRlidar is for Scaterring
897 Ratio from lidar signal
898
899 **Fig.3** Mean seasonal cycle of temperature (a), rain rate (4 lower lines, without circles)
900 and occurrence of precipitation (lines with circles) (b), downwards shortwave radiative
901 flux at the surface (c), downwards longwave radiative flux at the surface (d), sensible
902 heat flux (e) and latent heat flux (f) averaged over period d1 (solid lines) and d2 (dashed
903 lines). Black line is for observations, red is for CTRL and blue for SURF simulations (see
904 legend for details). Vertical bars indicate one standard deviation for observations
905
906 **Fig.4** Monthly mean of surface humidity as a function of monthly mean surface
907 temperature at 4 hours (03, 09, 15, 21 UTC). Colors represent the month of the year (see
908 correspondance on panel a). Each cross is for one month/one year from 2003-2008.
909 First row is for observations, second row for CTRL simulation, third row for SURF
910 simulation
911
912 **Fig.5** Seasonal cycle of occurrence of clouds computed from SR values in OBSd3 (a),
913 CTRLd3 (b) and SURFd3 (c). The occurrence is the number of cloudy profiles (SR>=5)
914 over the number of profiles for which SR>=0.01;
915
916 **Fig.6** SR histograms for lidar observations (first row) and simulated lidar profiles from
917 CTRL simulation (second row) and SURF simulation (third row) during winter (DJF-left
918 column) and summer (JJA-right column). The common dataset d3 is used. The white
919 vertical solid line indicates the limit between clouds (SR>=5) and clear or unclassified
920 atmopshere. The horizontal dashed lines indicate the low clouds layer.
921
922 **Fig.7:** a), b): Interannual variability of vertical profiles of cloud occurrence computed
923 from condensed water mixing ratio values in JJA in CTRLd2 (a) and SURFd2 (b); c) and
924 d): Diurnal cycle of vertical profiles of cloud occurrence computed from condensed
925 water values averaged over JJA for CTRLd2 (c) and SURFd2 (d). e: Diurnal cycle of the
926 difference between CTRLd2 and SURFd2 of the shortwave flux arriving at surface
927 averaged over JJA;
928

Fig.8 : Interannual variability of monthly mean surface temperature anomaly at SIRTA (solid line). Red is for CTRLd1, black is for OBSd1 and blue is for ERAI extracted at SIRTA grid point. Dashed lines indicate the inter-quantile range (between the 25% and 75% quantiles) of all data (all years) for each month. Dash-dotted lines indicate the maximum and miminum anomalies for each month of each year

Fig.9 Maximum temperature as a function of temperature quantile averaged over May to September. b) Same as a) for latent heat flux. c) Same as a) for downwards shortwave radiative flux at surface. The correspondance of the different lines is given by the legend.

Fig.10 a) Annual distribution of simulated total (red crosses) and clear sky (light blue circles) shortwave net fluxes and observed (black crosses) total one. b) SW simulated Net Cloud radiative effect (blue circles), downwards CRE (red crosses) and observed downwards CRE (black crosses). c) Seasonal cycle of simulated effective surface cloud albedo at 12 UTC in red solid line. Black solid line is for observed cloud albedo at 12UTC. Shaded areas represents the interannual variability of the monthly mean values. Dashed lines are for the monthly means of surface albedo (red for CTRLd1 and black for OBSd1). d) Simulated downwards α_{cloud} as a function of α_{cloud} bias (defined as simulated α_{cloud} minus observed one). e) Distribution of values with a given effective cloud albedo in winter. Black line is for observations, red line for simulation. f) same as e) in summer

Fig.11 a) Relationship between α_{cloud} and temperature anomaly of MJJAS from 2003 to 2011. Temperature anomaly is computed as the difference between the temperature of the day and the average temperature of this julian day over the 9 years and then stratified by α_{cloud} with 50 samples in each bin. The solid line corresponds to the 50th quantile and the shaded area covers the values between the 20th and 80th quantile. Red is for CTRLd1, black is for OBSd1. SURFd2 is in blue and the 20th and 80th are shown in dashed blue lines instead of shaded area. b) Relationship between α_{cloud} and the difference of temperature anomaly between simulation and observations. c) Probability of rain occurrence as a function of α_{cloud} . d) Relationship between rain rate (only wet days) and α_{cloud}

Fig. 12: Evolution of temperature as a function of surface conditions and net radiation. Blue circles corresponds to the SURF behavior in January (J), May (M) and July (Ju). Light green are for observations and Orange ones are for CTRL. The bigger the circle, the enhanced variability. Min and max values of temperature and amplitude of these values are mainly driven by large scale circulations.

968

Annex1: lidar equations

ATB_{tot} and ATB_{mol} are respectively the attenuated backscattered signals for particles and molecules (ATB_{tot}) and for molecules only (ATB_{mol}) and are given by (1) and (2):

$$ATB_{mol}(z) = \beta_{sca,mol}(z).e^{-2\eta \int_{z_{TOA}}^{z} \alpha_{sca,mol}(z).dz} \quad (1)$$

$$ATB_{tot}(z) = (\beta_{sca,part}(z) + \beta_{sca,mol}(z)).e^{-2\eta \int_{z_{TOA}}^{z} (\alpha_{sca,part}(z) + \alpha_{sca,mol}(z)).dz} \quad (2)$$

Where $\beta_{sca,part}$, $\beta_{sca,mol}$ are lidar backscatter coefficients (m^{-1} sr^{-1}) and $\alpha_{sca,part}$ and $\alpha_{sca,mol}$ attenuation coefficients (m^{-1}) for particles (clouds, aerosols) and molecules. η is a multiple scattering coefficient that depends both on lidar characteristics and size, shape and density of particles. It is about 0.7 for CALIPSO (Winker, 2003; Chepfer et al., 2008). The ATB_{mol} and ATB_{tot} products are averaged vertically to obtain SR over 40 layers (Chepfer et al. 2008 and 2010). SR is given by (3):

$$SR = \frac{ATB_{tot}}{ATB_{mol}} \quad (3)$$

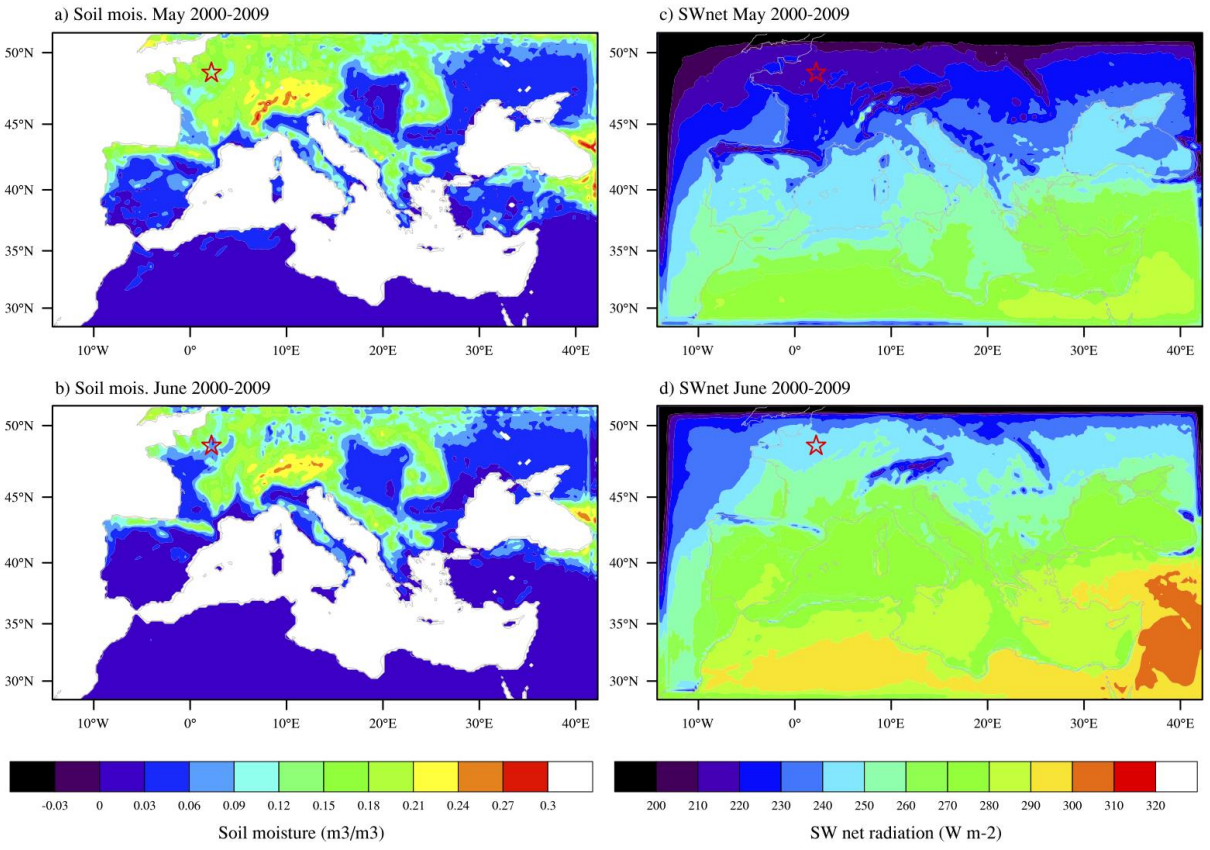

Figure 1: Domain of the simulation and location of SIRTA site (red star). Colormap presents a) the soil moisture of May averaged over 2000-2009; (b) same as a) for June; c) the shortwave surface net radiation of May averaged over 2000-2009; d) same as c) for June.

985

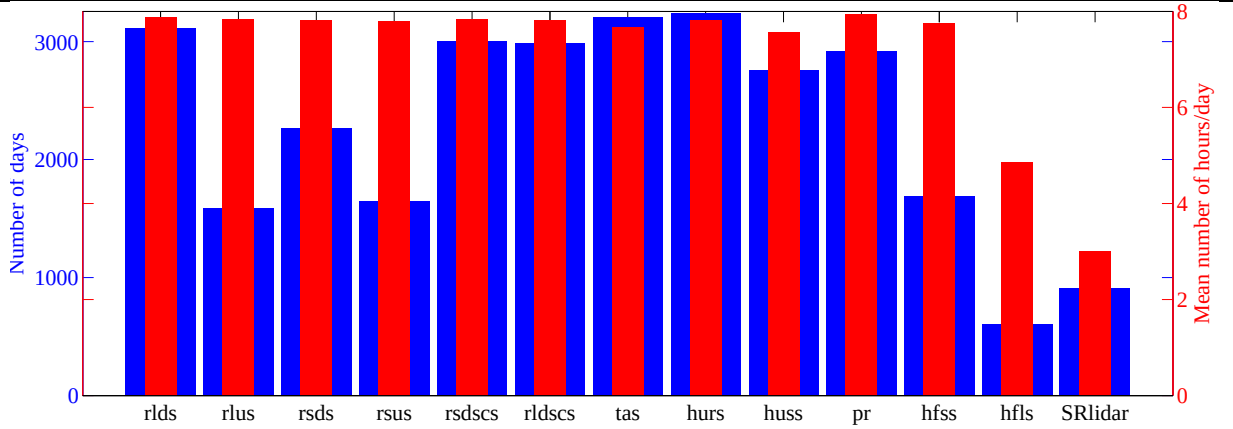

Figure 2: Blue histograms indicate the number of days with measurements (the maximum being 3256 over the period of the study) for each parameter. Red bars indicate the average number of hours per day with measurements (only considering 0, 3, 6, 9, 12, 15, 18 and 21 UTC). rlds stands for 'radiative longwave downwards at surface', rlus is the same but upwards, rsds and rsus are the same for shortwave and rsdscs/rldscs are for clear sky fluxes. tas is for temperature at 2-m. hurs and huss are respectively relative and specific humidity at 2-m, pr is for precipitation, hfss and hfls are for sensible and latent heat fluxes respectively. SRlidar is for Scaterring Ratio from lidar signal

986
987

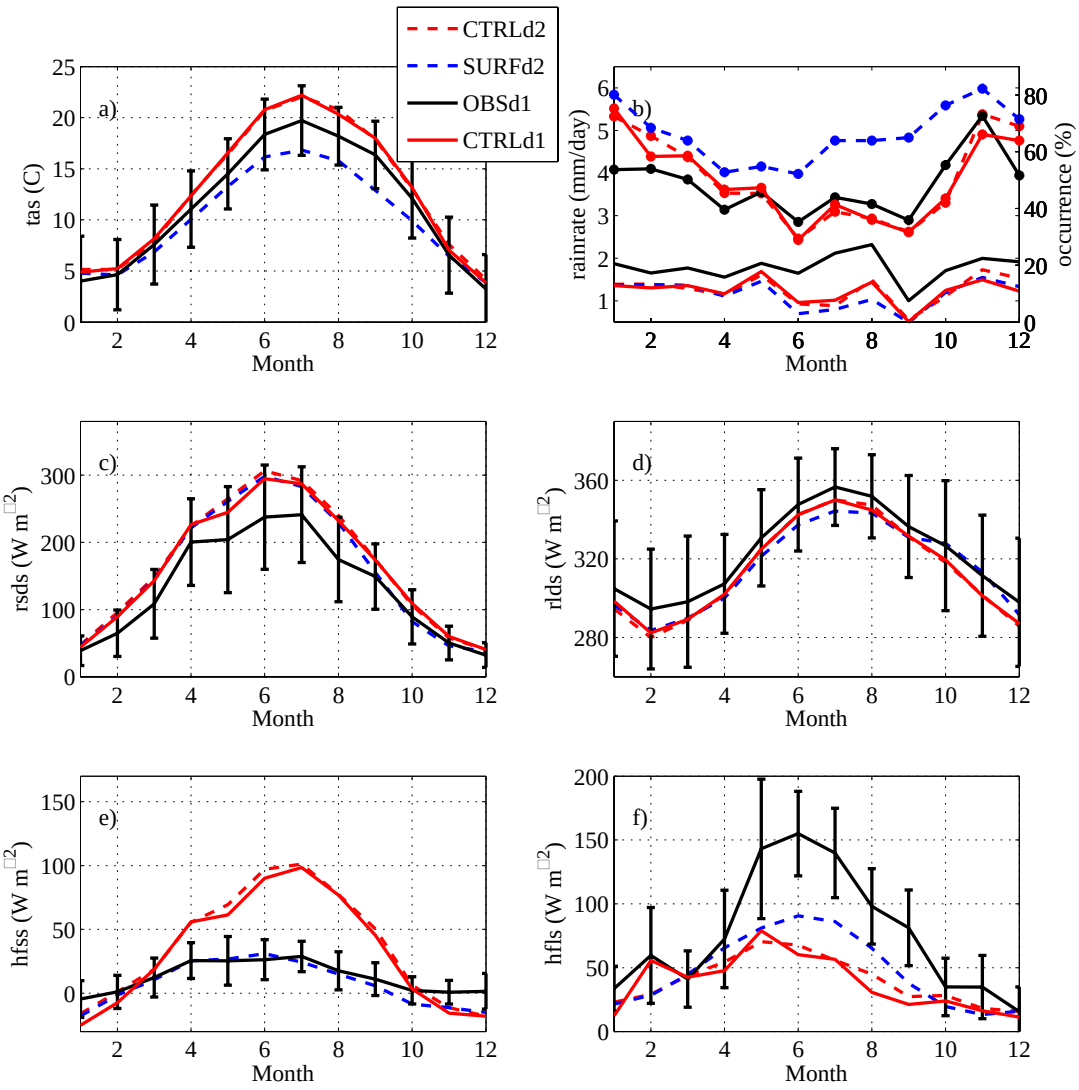

Figure 3: mean seasonal cycle of temperature (a), rainrate (4 lower lines, without circles) and occurrence of precipitation (lines with circles) (b), downwards shortwave radiative flux at the surface (c), downwards longwave radiative flux at the surface (d), sensible heat flux (e) and latent heat flux (f) averaged over period d1 (solid lines) and d2 (dashed lines). Black line is for observations, red is for CTRL and blue for SURF simulations (see legend for details). Vertical bars indicate one standard deviation for observations.

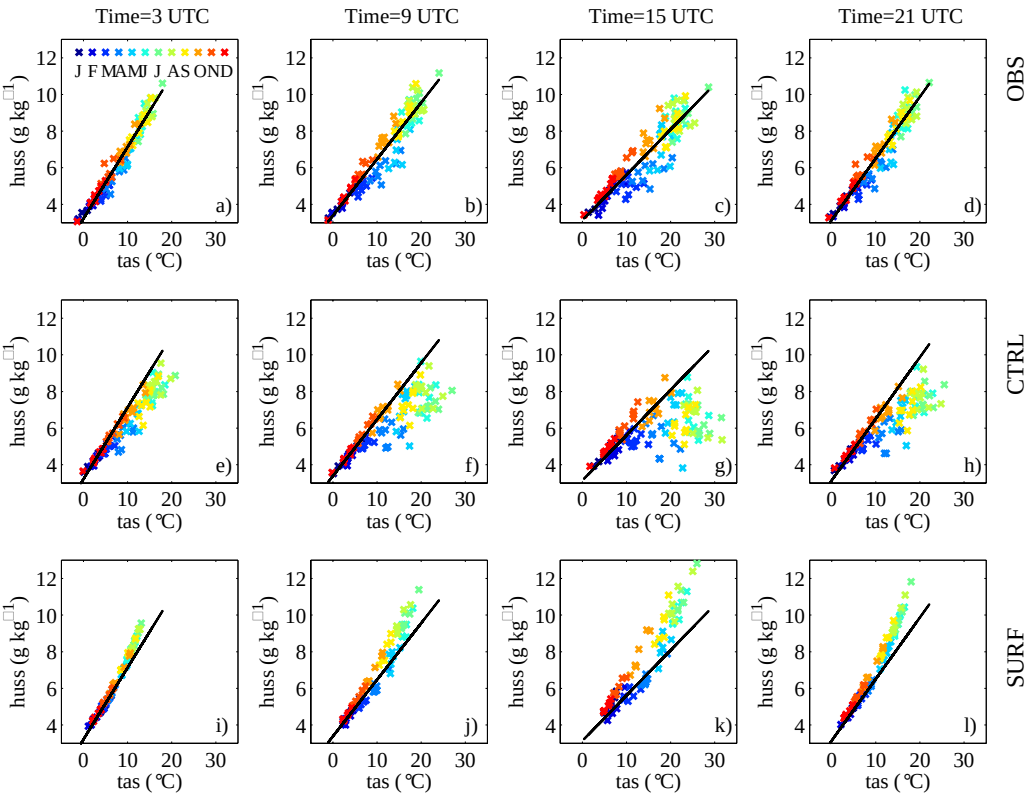

Figure 4: monthly mean of surface humidity as a function of monthly mean surface temperature at 4 hours (03, 09, 15, 21 UTC). Colors represent the month of the year (see correspondance on panel a). Each cross is for one month/one year from 2003-2008. First row is for observations, second row for CTRL simulation, third row for SURF simulation.

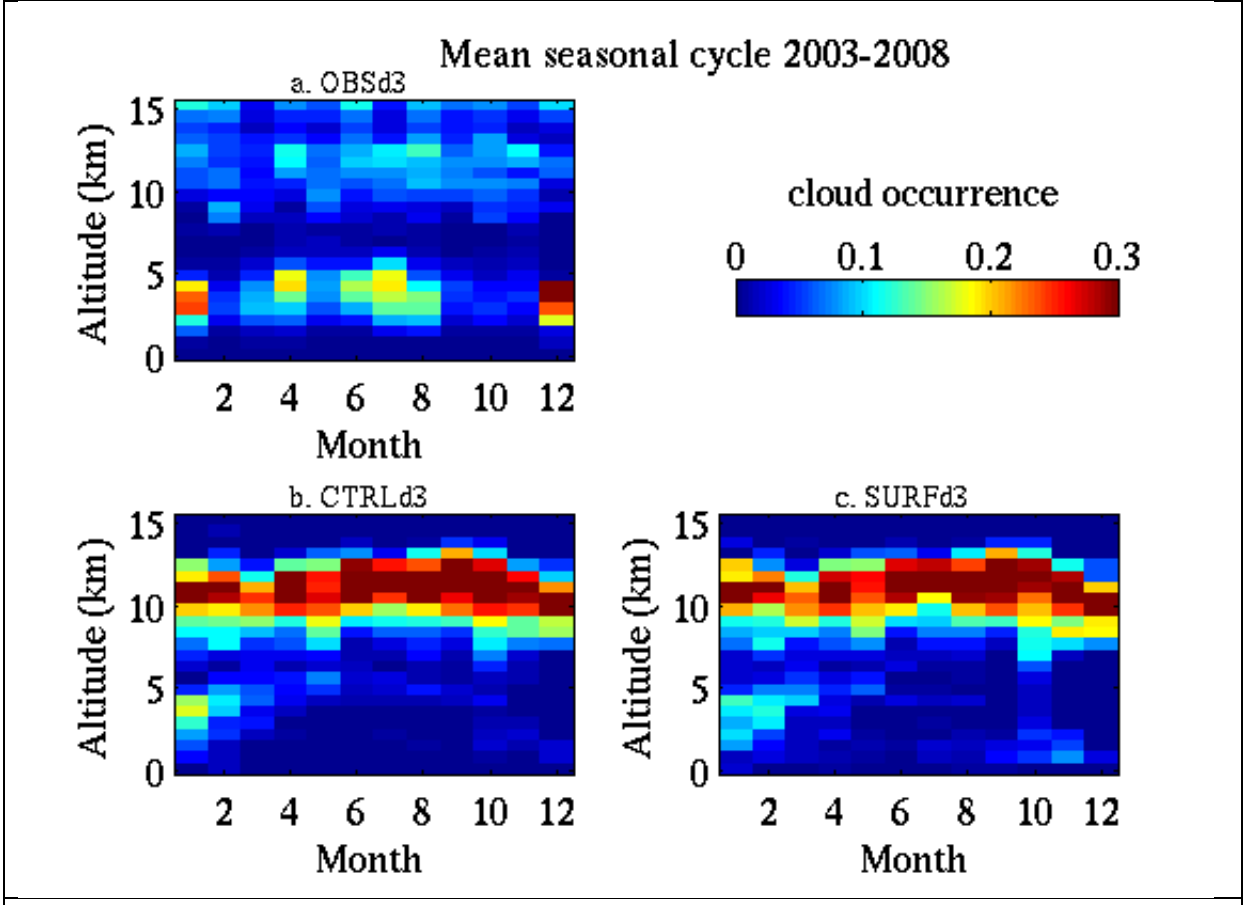

Figure 5: Seasonal cycle of occurrence of clouds computed from SR values in OBSd3 (a), CTRLd3 (b) and SURFd3 (c). The occurrence is the number of cloudy profiles (SR>=5) over the number of profiles for which SR>=0.01;

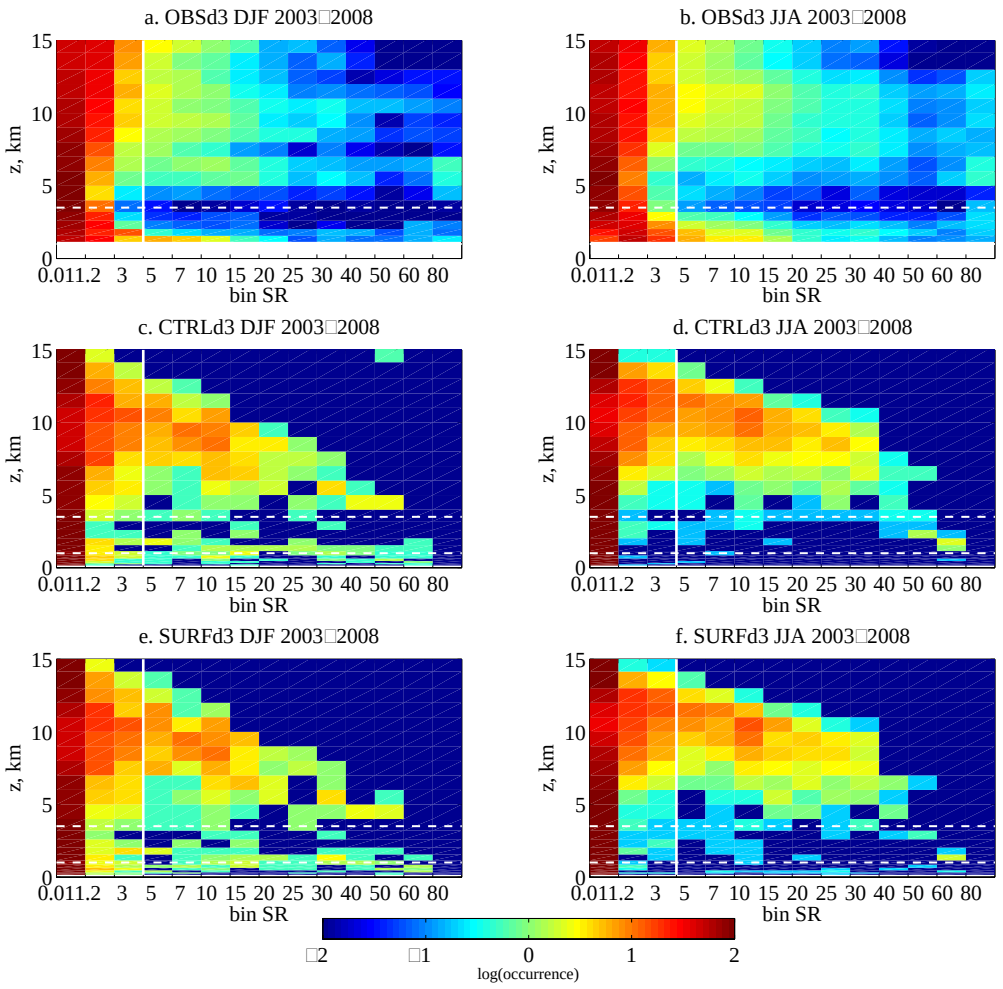

Figure 6: SR histograms for lidar observations (first row) and simulated lidar profiles from CTRL simulation (second row) and SURF simulation (third row) during winter (DJF-left column) and summer (JJA-right column). The common dataset d3 is used. The white vertical solid line indicates the limit between clouds (SR>=5) and clear or unclassified atmopshere. The horizontal dashed lines indicate the low clouds layer.

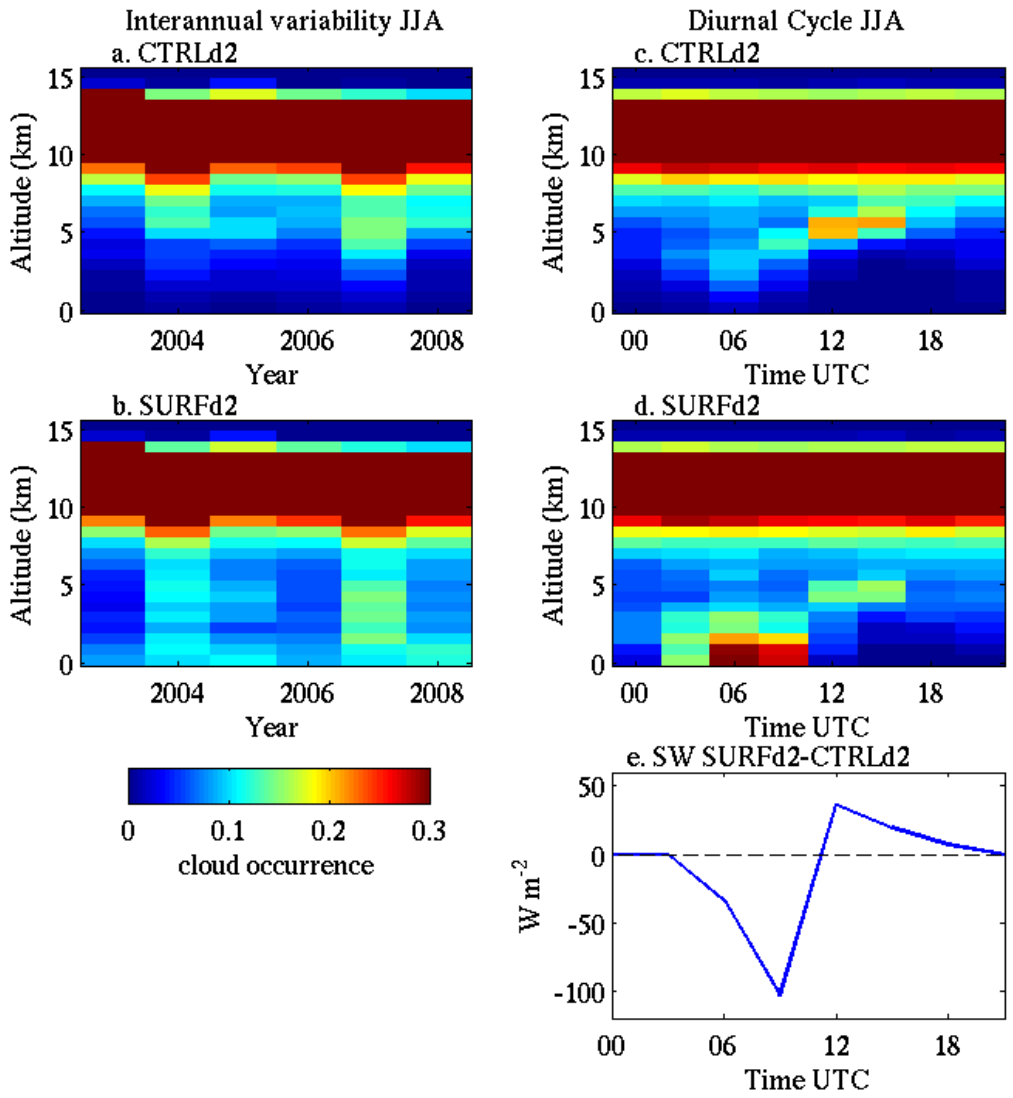

Figure 7: a), b): Interannual variability of vertical profiles of cloud occurrence computed from condensed water mixing ratio values in JJA in CTRLd2 (a) and SURFd2 (b); c) and d): Diurnal cycle of vertical profiles of cloud occurrence computed from condensed water values averaged over JJA for CTRLd2 (c) and SURFd2 (d). e: Diurnal cycle of the difference between CTRLd2 and SURFd2 of the shortwave flux arriving at surface averaged over JJA;

1000
1001

1002

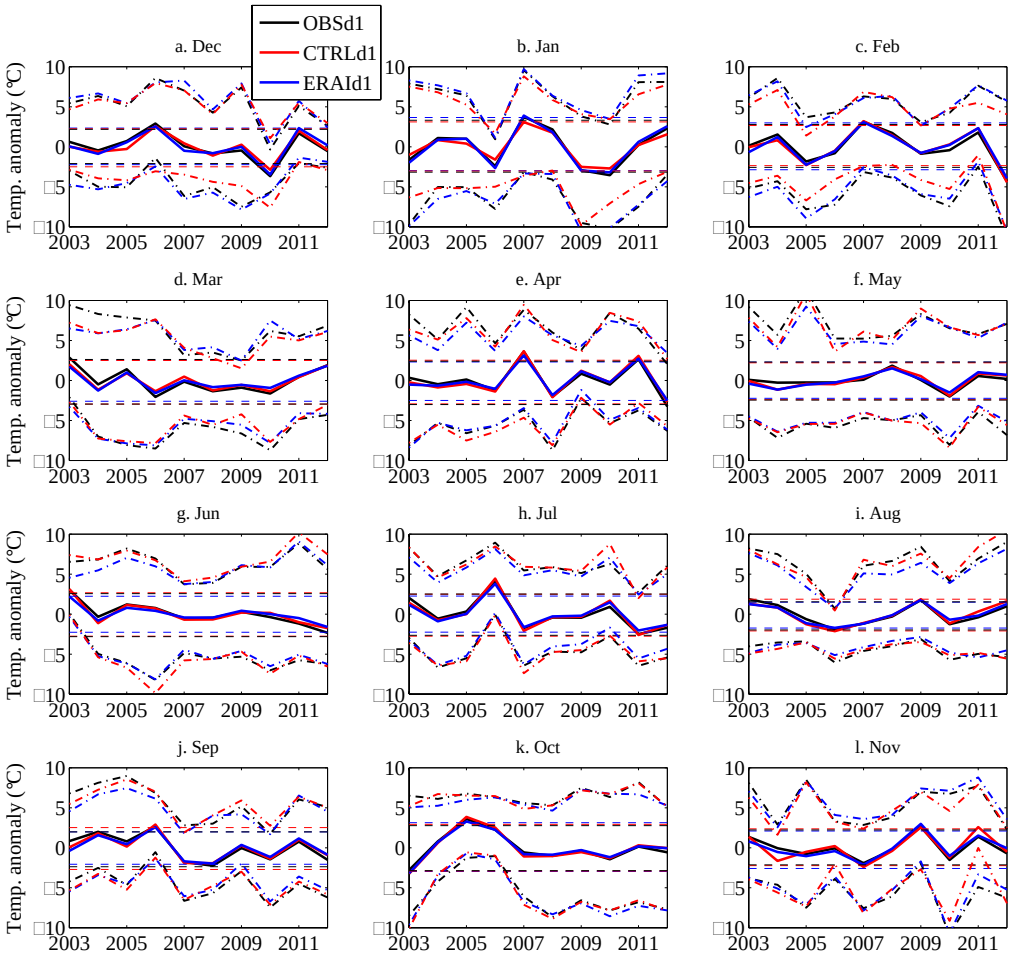

Figure 8: Interannual variability of monthly mean surface temperature anomaly at SIRTA (solid line). Red is for CTRLd1, black is for OBSd1 and blue is for ERAI extracted at SIRTA grid point. Dashed lines indicate the inter-quantile range (between the 25% and 75% quantiles) of all data (all years) for each month. Dash-dotted lines indicate the maximum and miminum anomalies for each month of each year.

1003
1004

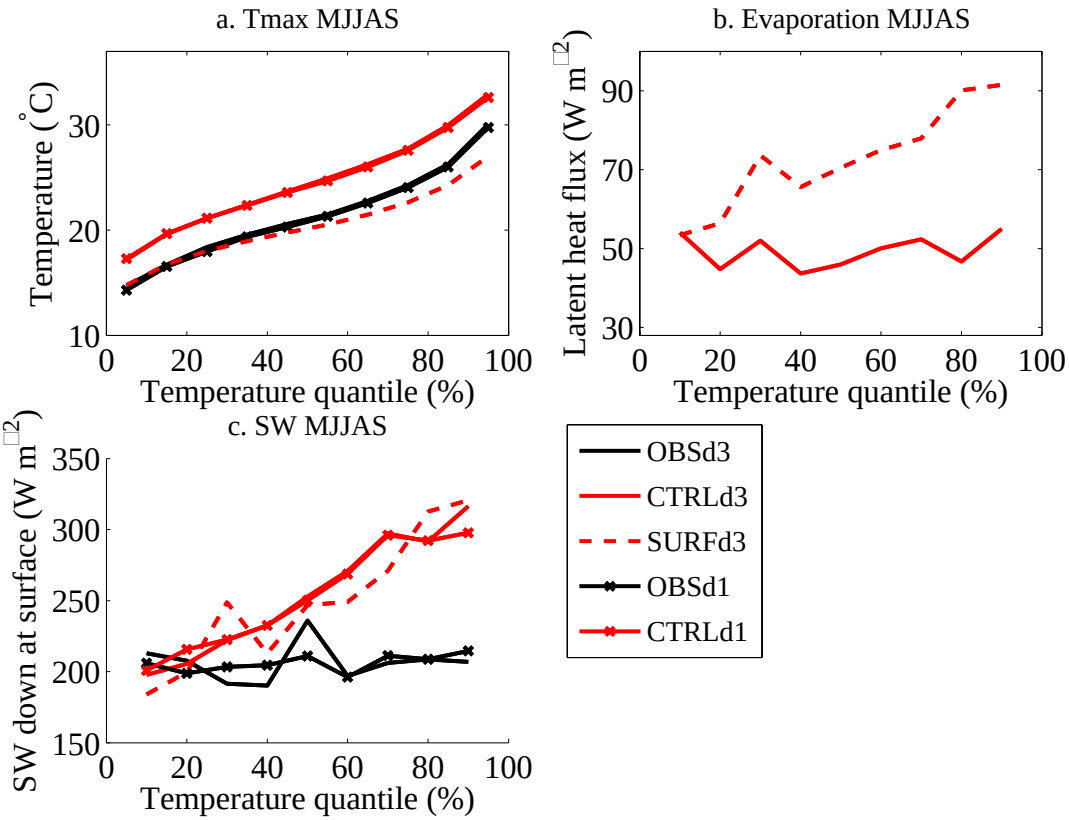

Figure 9: Maximum temperature as a function of temperature quantile averaged over May to September. b) Same as a) for latent heat flux. c) Same as a) for downwards shortwave radiative flux at surface. The correspondance of the different lines is given by the legend.

1007

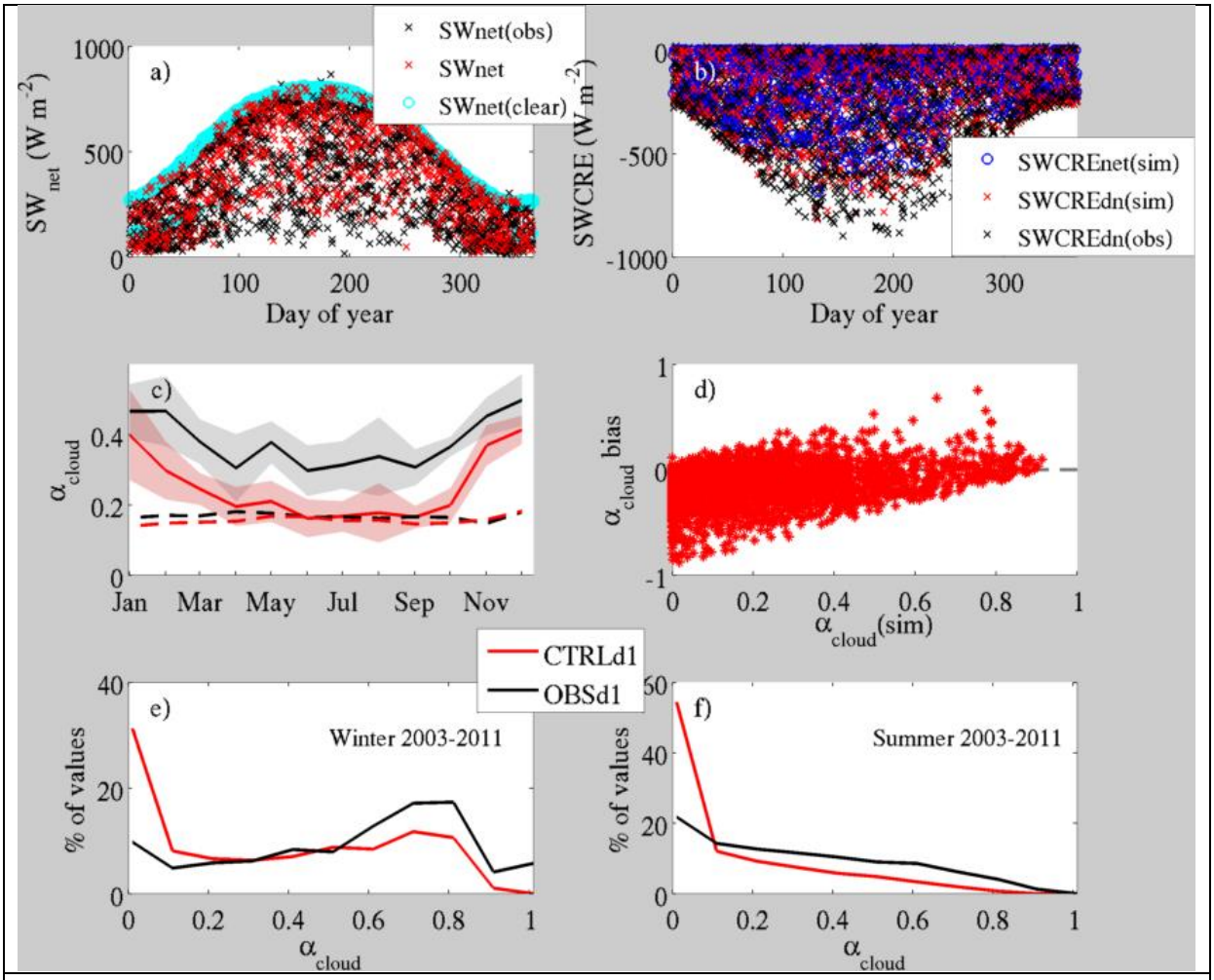

Figure 10: a) Annual distribution of simulated total (red crosses) and clear sky (light blue circles) shortwave net fluxes and observed (black crosses) total one. b) SW simulated Net Cloud radiative effect (blue circles), downwards CRE (red crosses) and observed downwards CRE (black crosses). c) Seasonal cycle of simulated effective surface cloud albedo at 12 UTC in red solid line. Black solid line is for observed cloud albedo at 12UTC. Shaded areas represents the interannual variability of the monthly mean values. Dashed lines are for the monthly means of surface albedo (red for CTRLd1 and black for OBSd1). d) Simulated downwards α_{cloud} as a function of α_{cloud} bias (defined as simulated α_{cloud} minus observed one). e) Distribution of values with a given effective cloud albedo in winter. Black line is for observations, red line for simulation. f) same as e) in summer.

1008
1009

1010

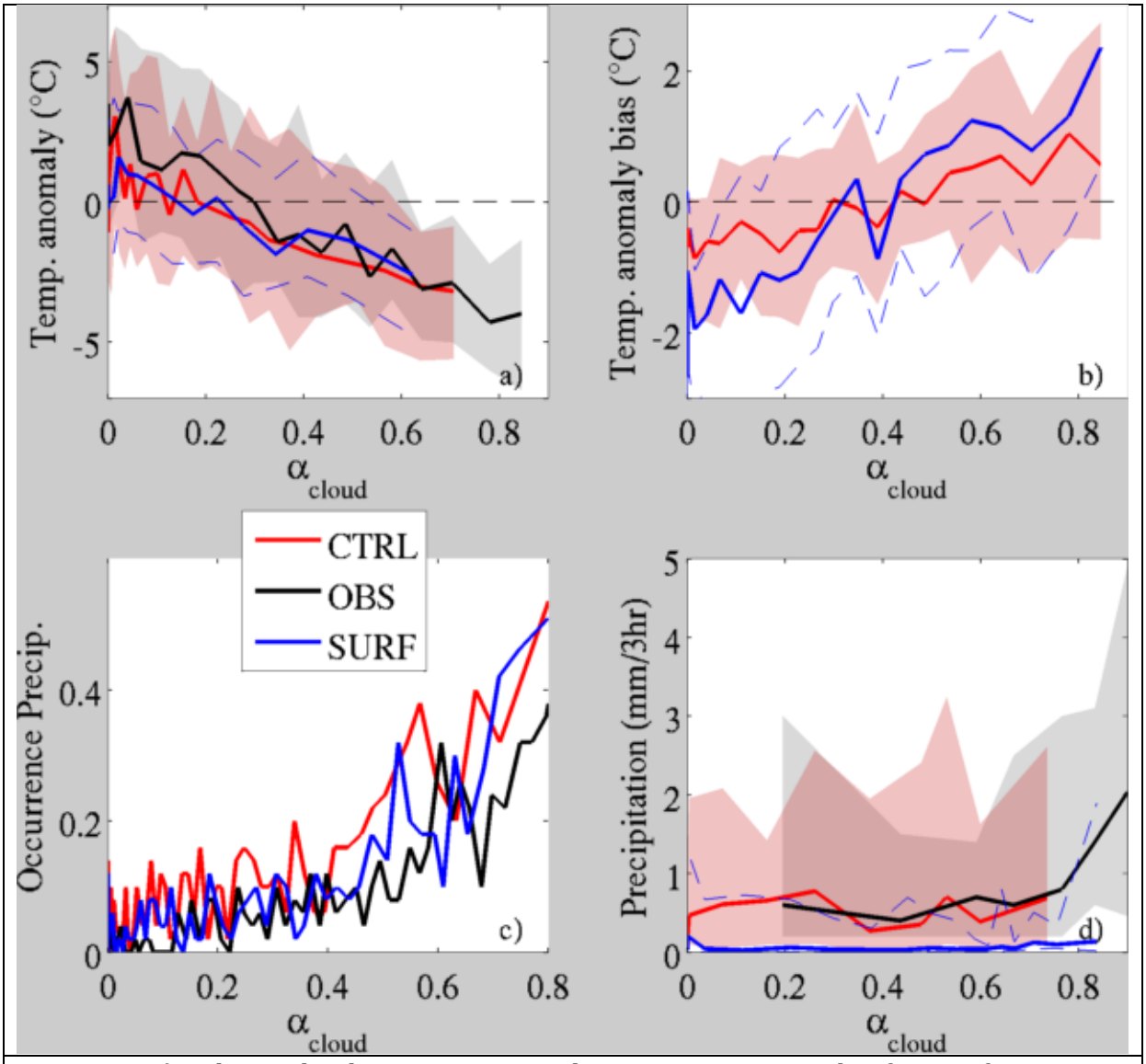

Figure 11: a) Relationship between α_{cloud} and temperature anomaly of MJJAS from 2003 to 2011. Temperature anomaly is computed as the difference between the temperature of the day and the average temperature of this julian day over the 9 years and then stratified by α_{cloud} with 50 samples in each bin. The solid line corresponds to the 50th quantile and the shaded area covers the values between the 20th and 80th quantile. Red is for CTRLd1, black is for OBSd1. SURFd2 is in blue and the 20th and 80th are shown in dashed blue lines instead of shaded area. b) Relationship between α_{cloud} and the difference of temperature anomaly between simulation and observations. c) Probability of rain occurrence as a function of α_{cloud} . d) Relationship between rain rate (only wet days) and α_{cloud}.

1011
1012

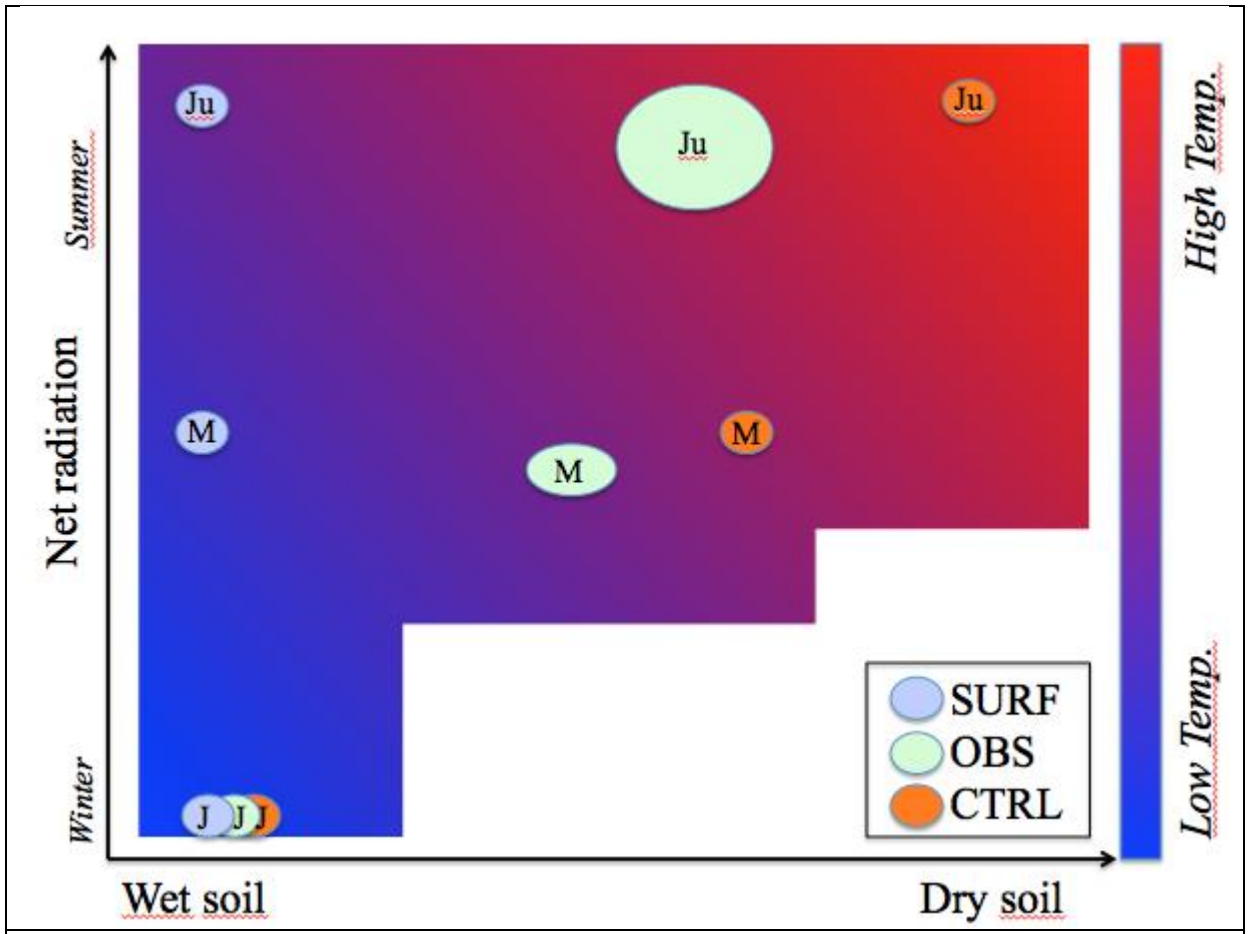

Figure 12: Evolution of temperature as a function of surface conditions and net radiation. Blue circles corresponds to the SURF behavior in January (J), May (M) and July (Ju). Light green are for observations and Orange ones are for CTRL. The bigger the circle, the enhanced variability. Min and max values of temperature and amplitude of these values are mainly driven by large scale circulations.

1013
1014

Figure 1

Click here to download Figure fig1_final.png

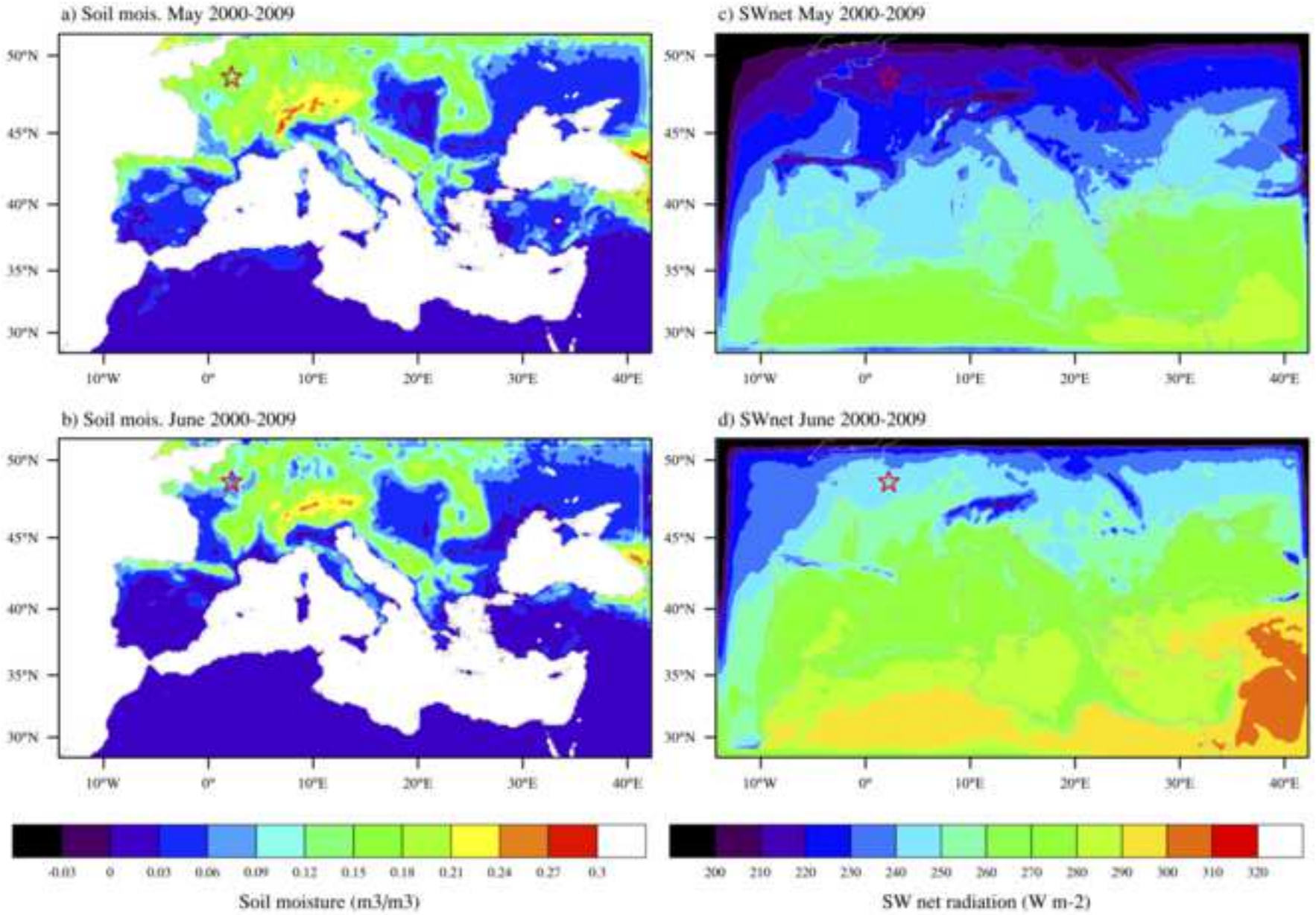

Figure 2

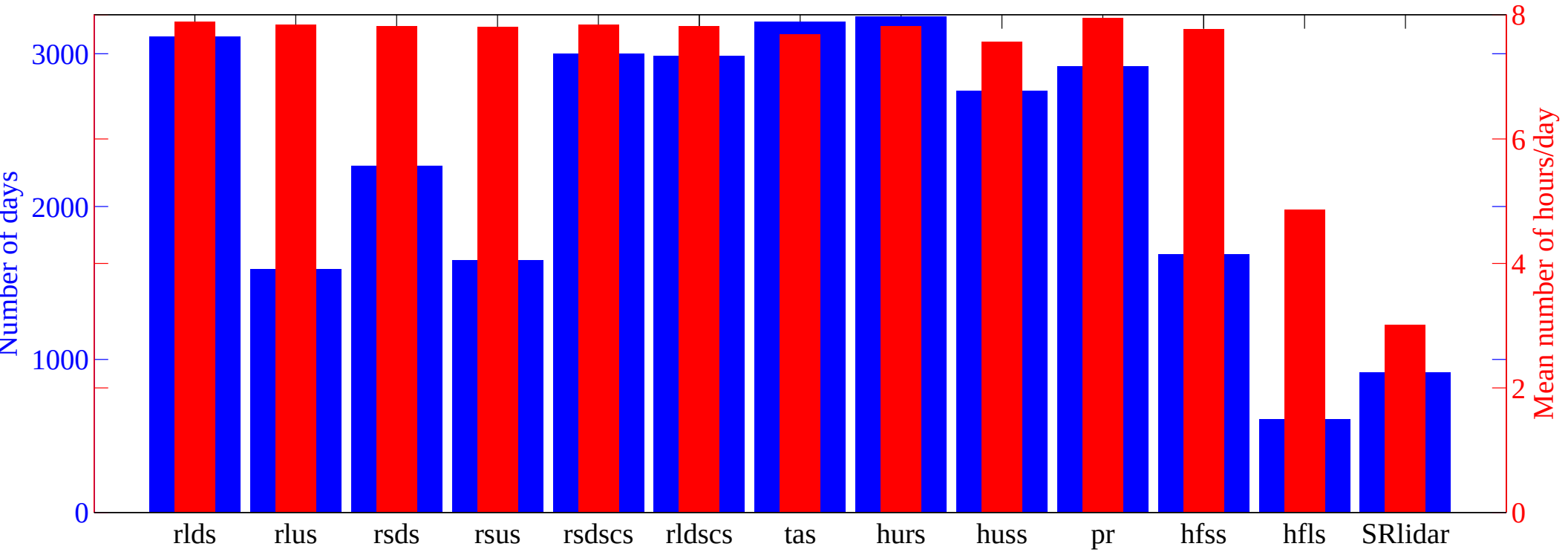
Number of days
Mean number of hours/day
0
1000
2000
3000
0
2
4
6
8
rlds
rlus
rsds
rsus
rsdscs
rldscs
tas
hurs
huss
pr
hfss
hfls
SRlidar

Figure 3

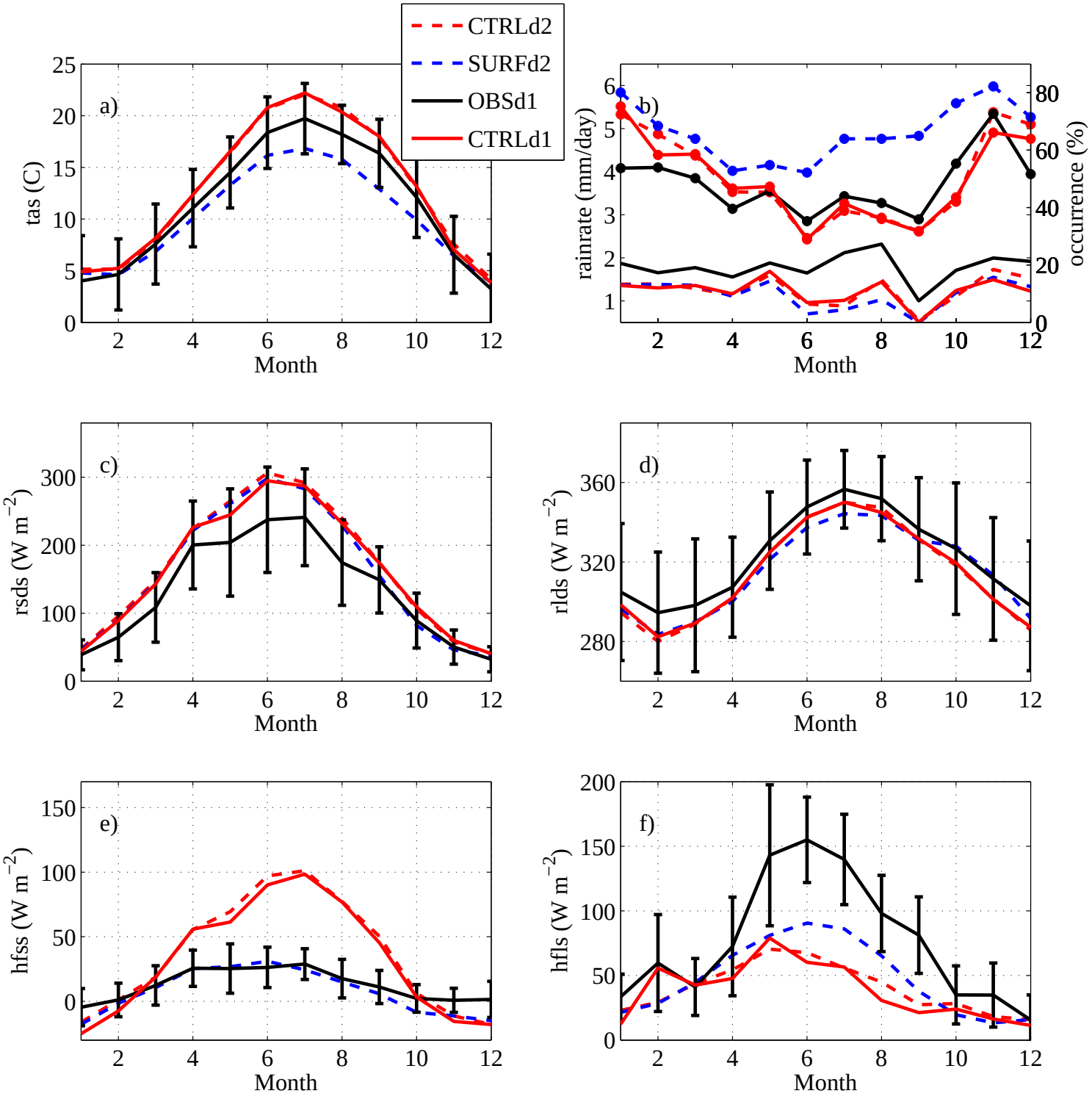
CTRLd2
SURFd2
OBSd1
CTRLd1
a)
tas (C)
Month
b)
rainrate (mm/day)
occurrence (%)
Month
c)
rsds (W m^{-2})
Month
d)
rlds (W m^{-2})
Month
e)
hfss (W m^{-2})
Month
f)
hfls (W m^{-2})
Month

Figure 4

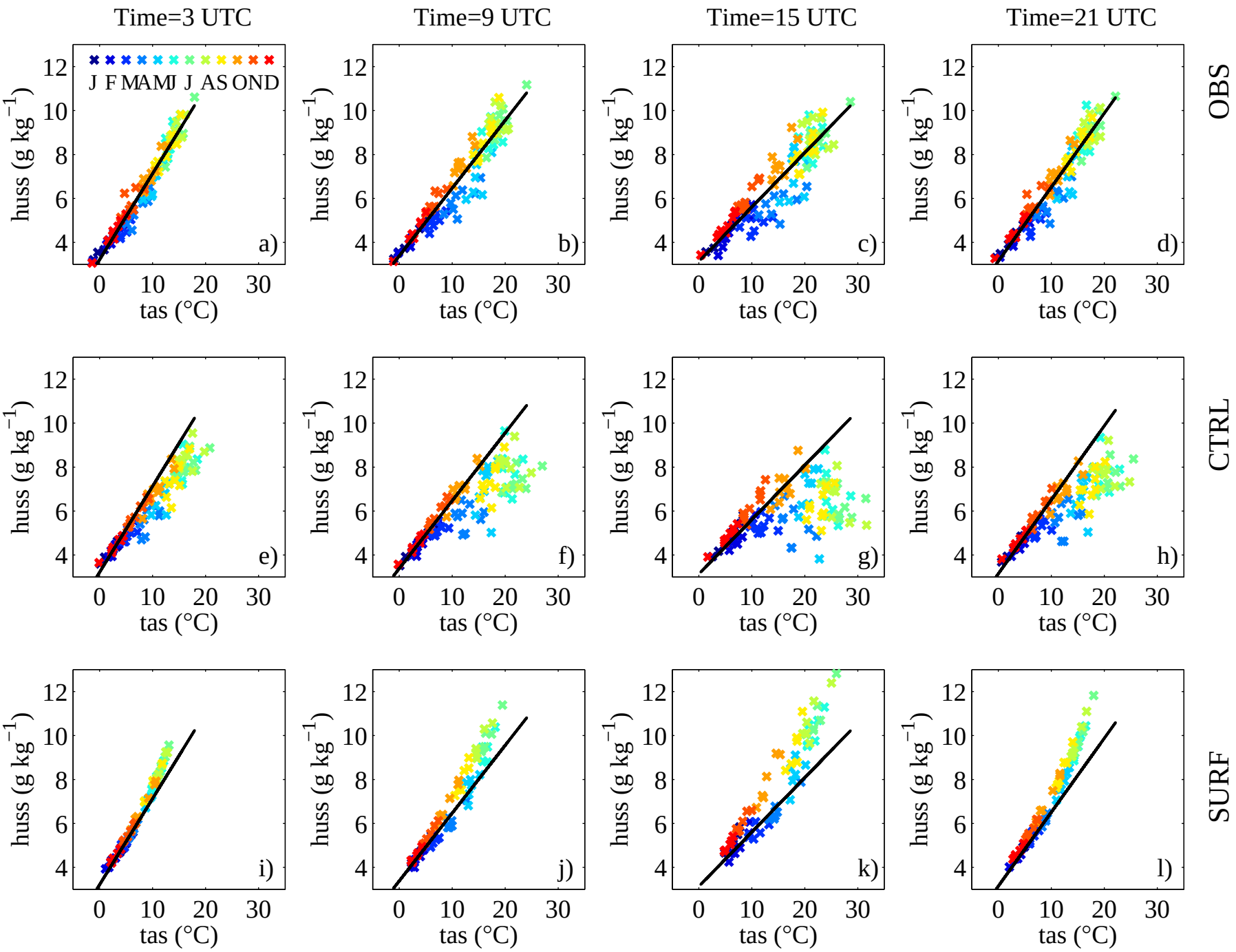
Time=3 UTC
Time=9 UTC
Time=15 UTC
Time=21 UTC
J F MAMJ J AS OND
huss (g kg^{-1})
tas (°C)
a)
b)
c)
d)
e)
f)
g)
h)
i)
j)
k)
l)
OBS
CTRL
SURF

Figure 5

Click here to download Figure fig5_final.tif

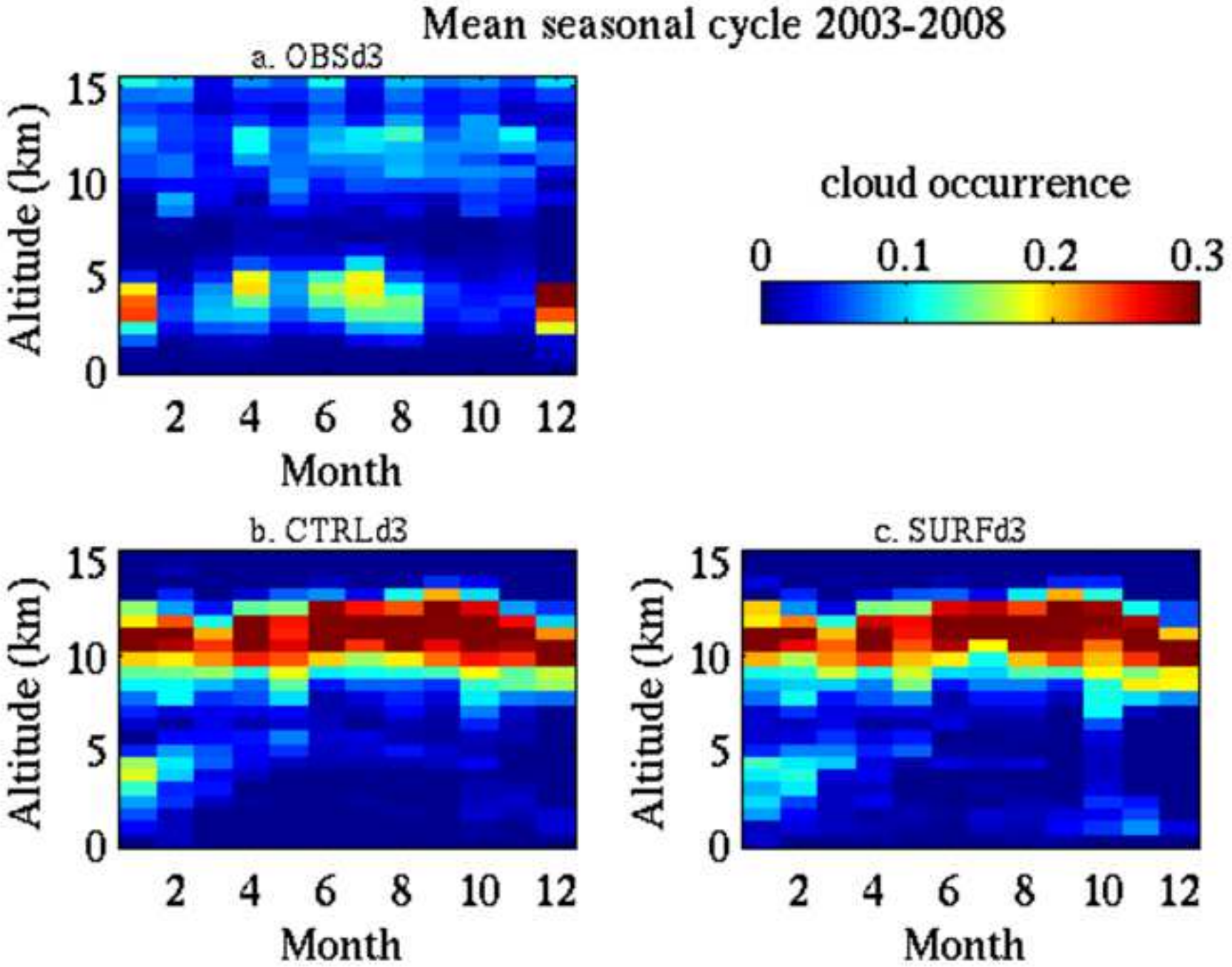

Figure 6

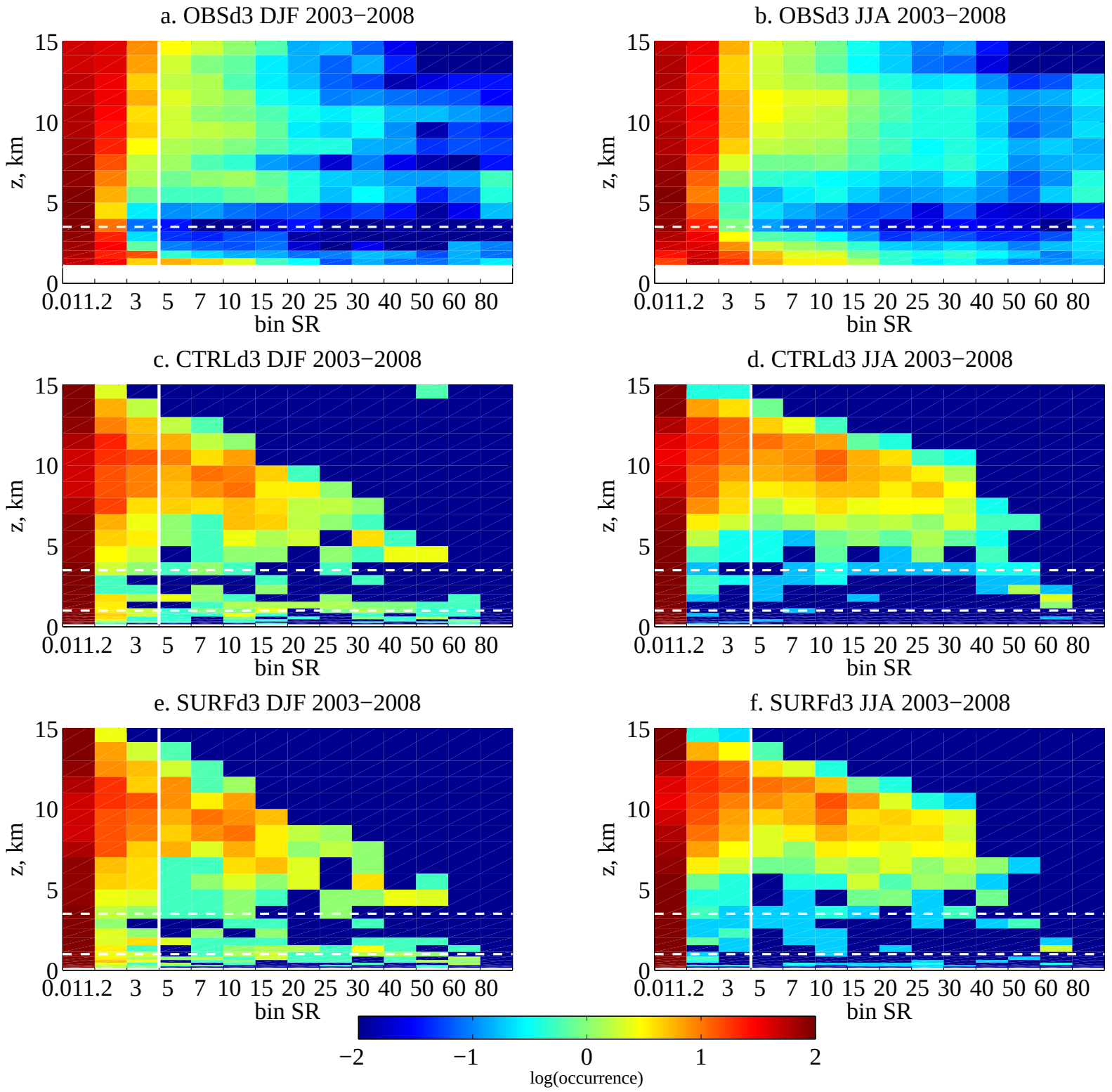
a. OBSd3 DJF 2003−2008
b. OBSd3 JJA 2003−2008
c. CTRLd3 DJF 2003−2008
d. CTRLd3 JJA 2003−2008
e. SURFd3 DJF 2003−2008
f. SURFd3 JJA 2003−2008
z, km
0
5
10
15
0.01 1.2 3 5 7 10 15 20 25 30 40 50 60 80
bin SR
−2 −1 0 1 2
log(occurrence)

Figure 7

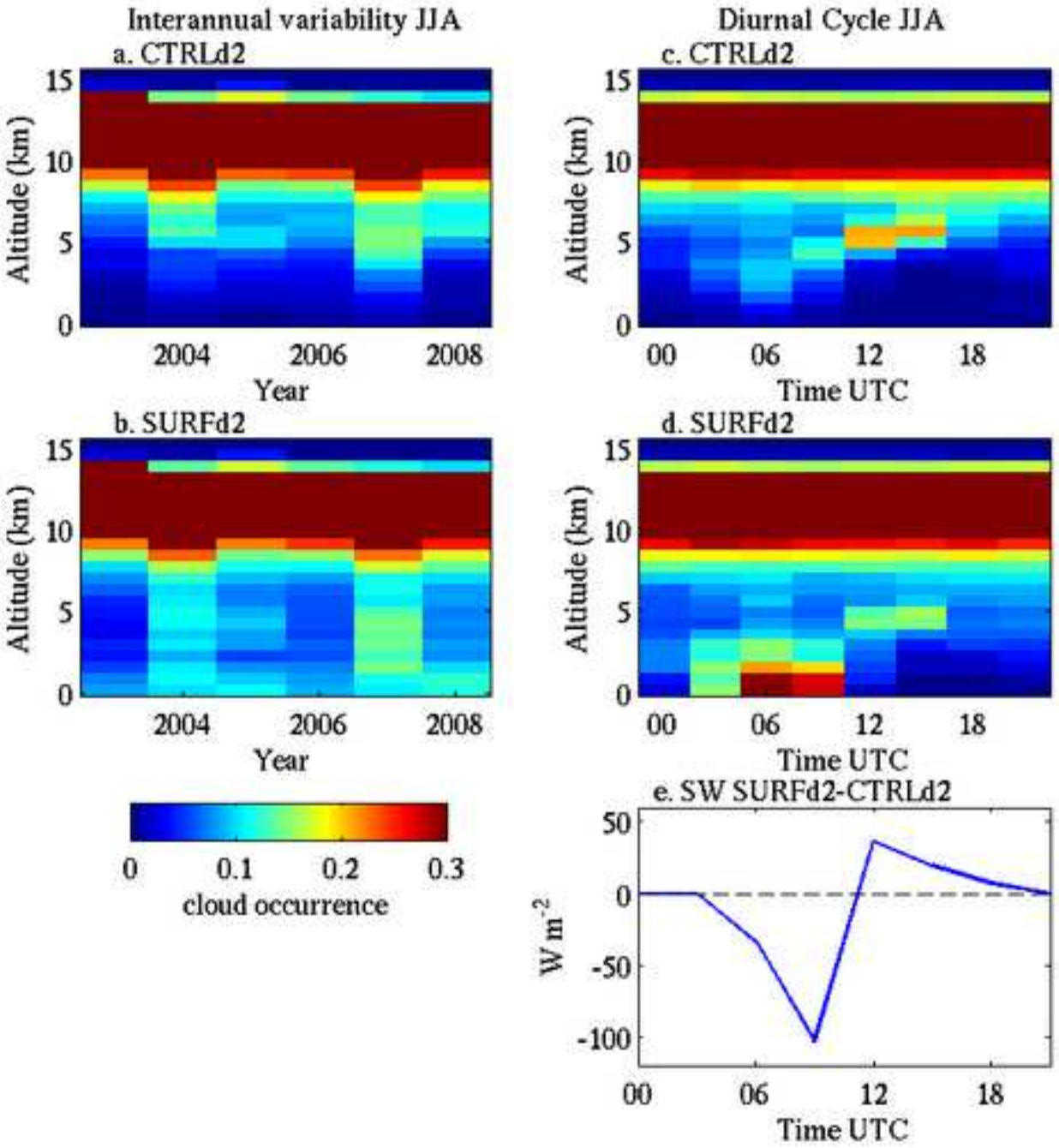

Figure 8

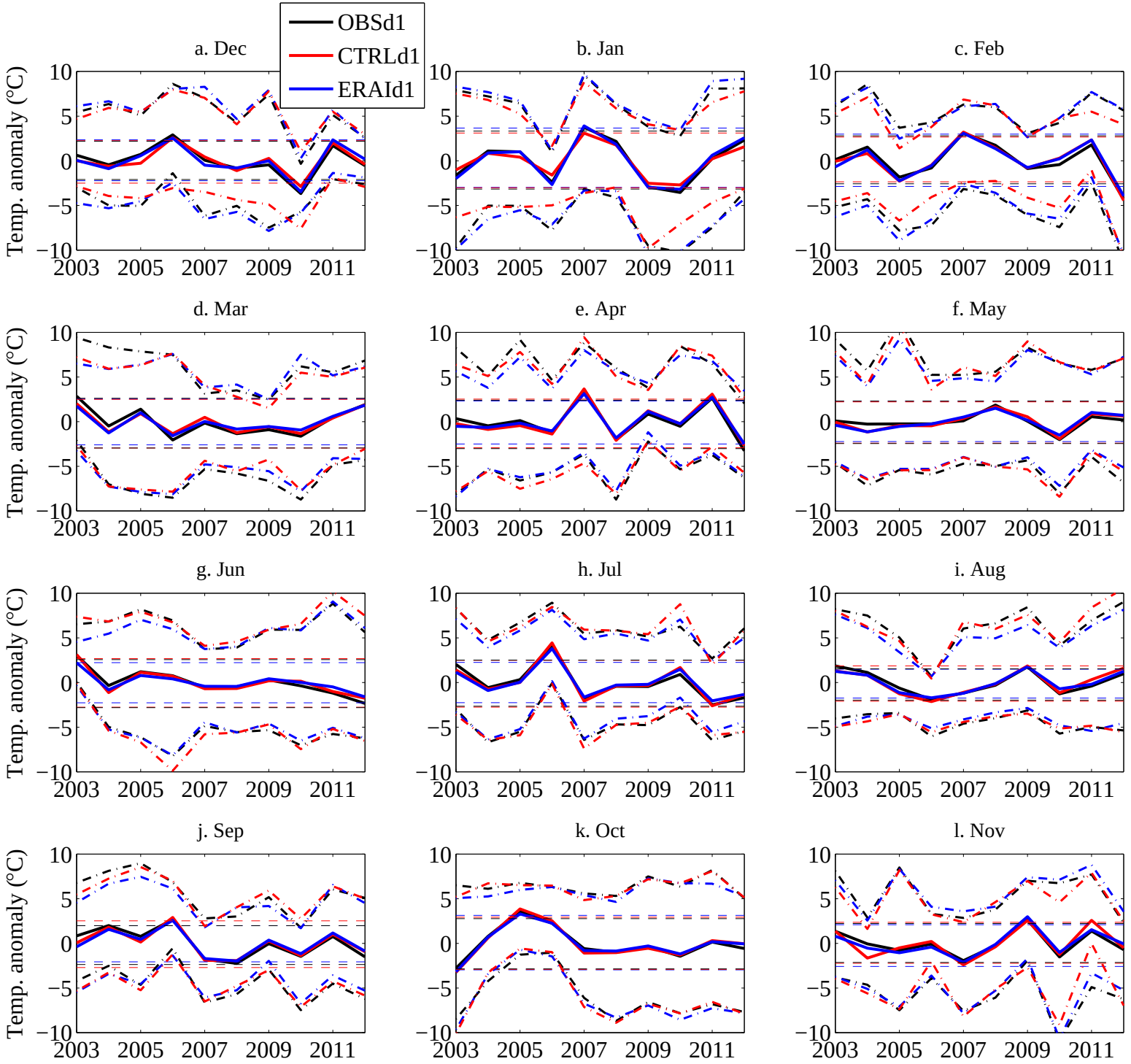
OBSd1
CTRLd1
ERAId1
a. Dec
b. Jan
c. Feb
d. Mar
e. Apr
f. May
g. Jun
h. Jul
i. Aug
j. Sep
k. Oct
l. Nov
Temp. anomaly (°C)
10
5
0
−5
−10
2003
2005
2007
2009
2011

Figure 9

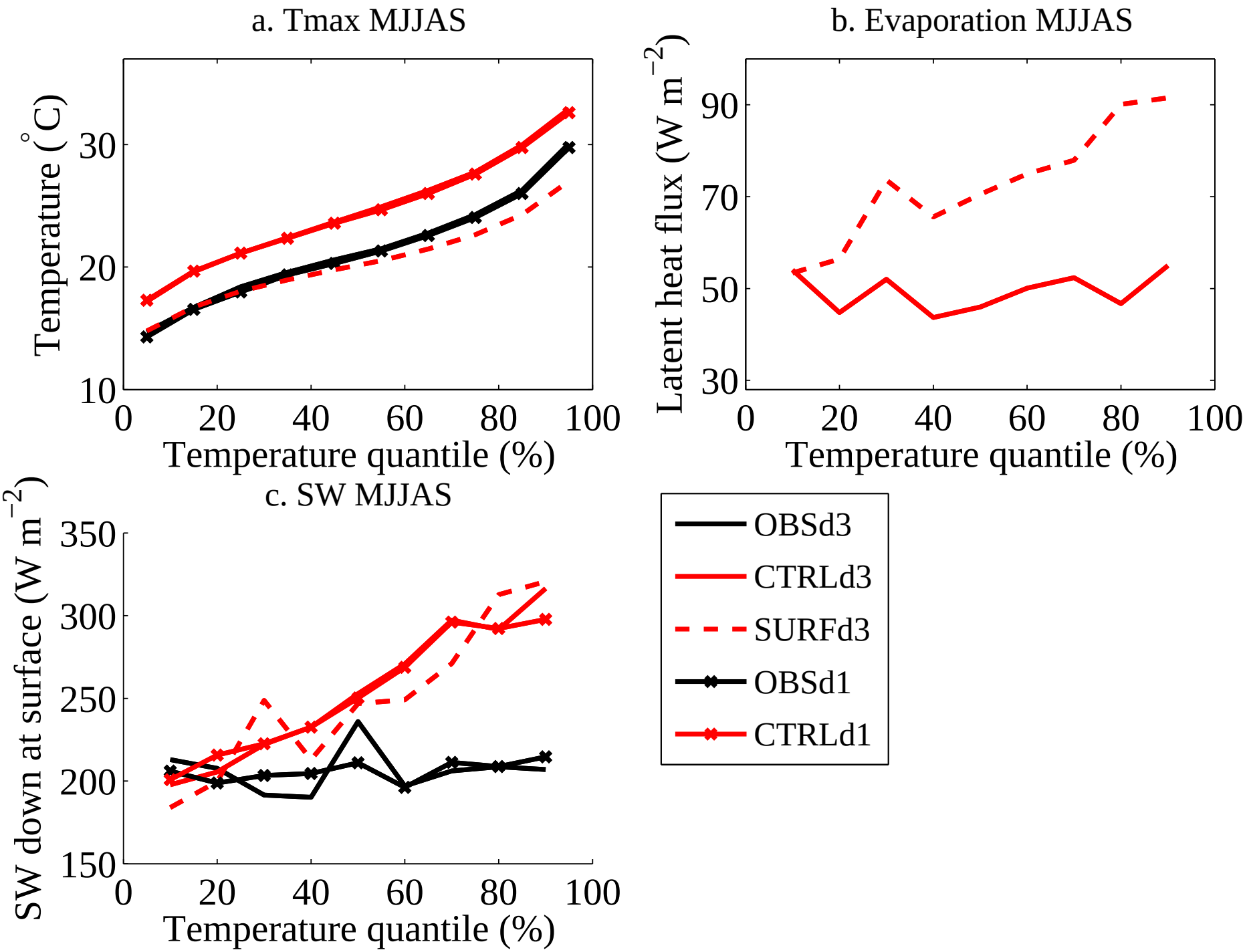
a. Tmax MJJAS
Temperature (°C)
10
20
30
0
20
40
60
80
100
Temperature quantile (%)
b. Evaporation MJJAS
Latent heat flux (W m−2)
30
50
70
90
0
20
40
60
80
100
Temperature quantile (%)
c. SW MJJAS
SW down at surface (W m−2)
150
200
250
300
350
0
20
40
60
80
100
Temperature quantile (%)
OBSd3
CTRLd3
SURFd3
OBSd1
CTRLd1

Figure 10

Click here to download Figure fig10_final.tif

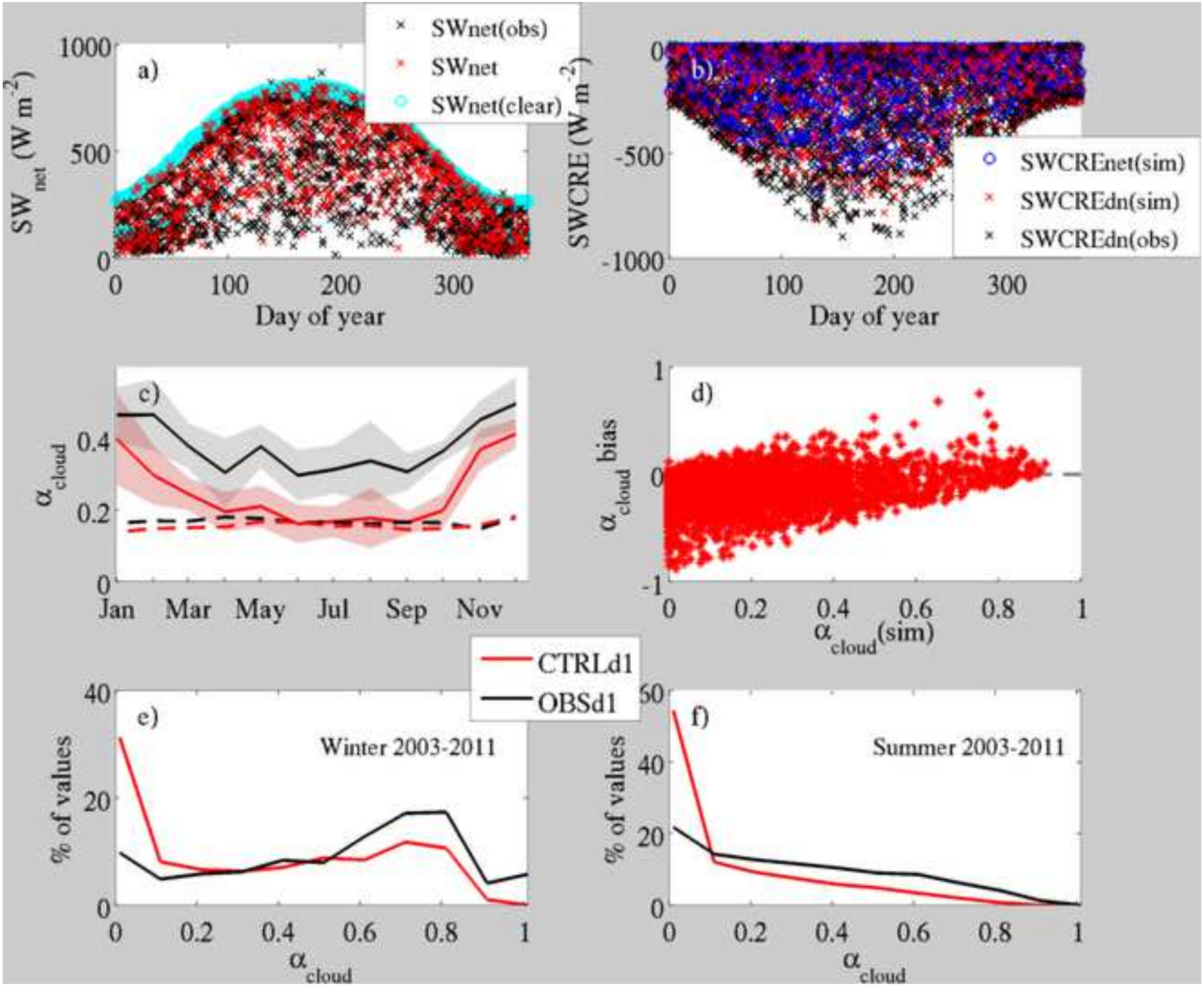

Figure 11

Click here to download Figure fig11_final.tif

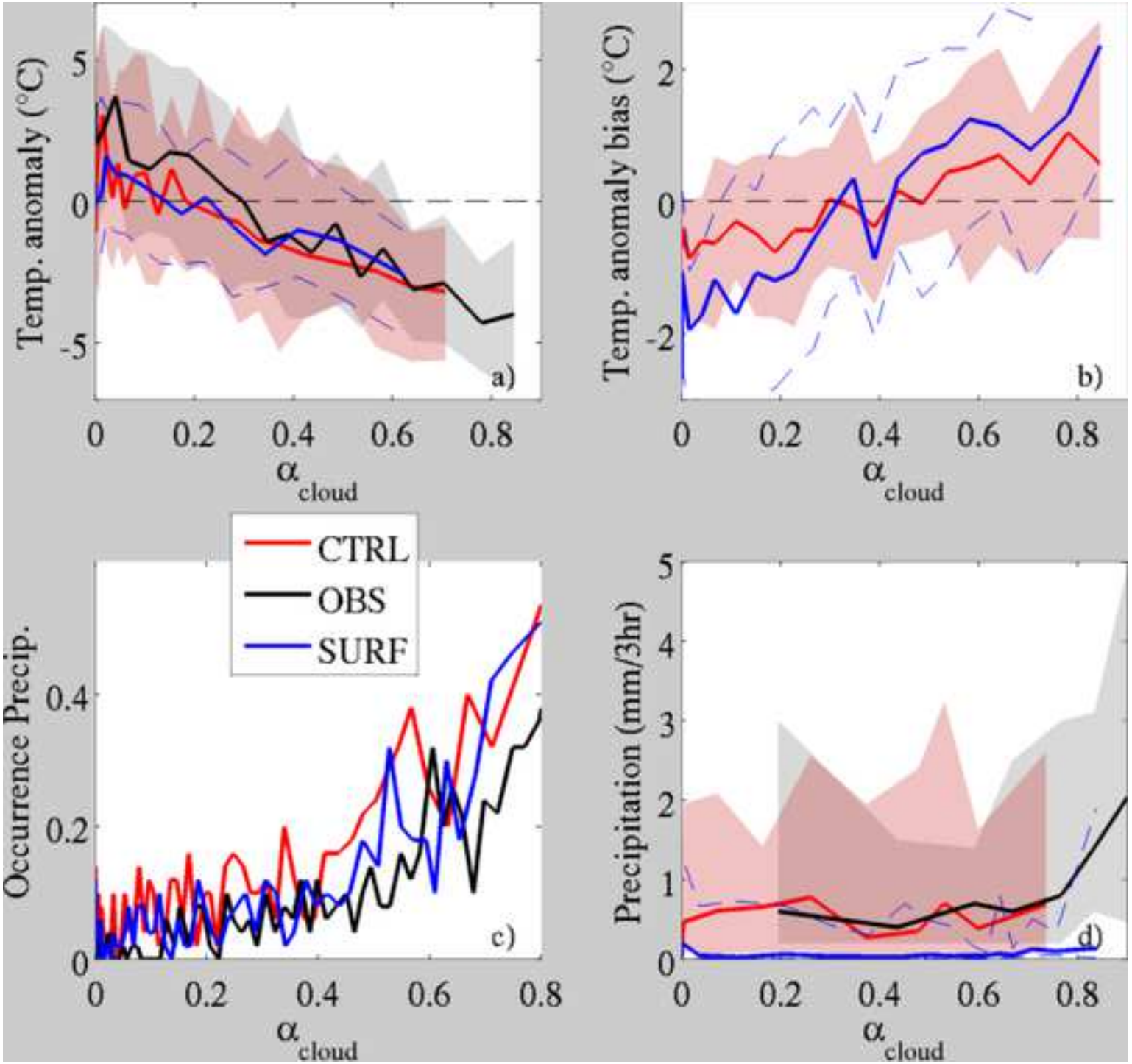

Figure 12

Click here to download Figure fig12_final.png